Rietveld refined structural, morphological, Raman and magnetic investigations of superparamagnetic Zn–Co nanospinel ferrites prepared by cost-effective co-precipitation route

Published: 01 June 2021

Volume 127, article number 480, (2021) Cite this article

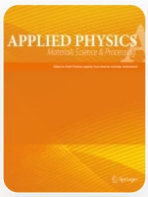

Applied Physics A

Aims and scope

Submit manuscript

Deepali D. Andhare, Supriya R. Patade, Swapnil A. Jadhav, Sandeep B. Somvanshi & K. M. Jadhav

Abstract

Zn^{2+}-substituted cobalt ferrites (Co-ferrite) having the chemical formula $Co_{1-x}Zn_xFe_2O_4$ (x = 0.0, 0.5 and 1.0) were fabricated by a co-precipitated wet chemical route. The analysis of

weight loss percentage with spinel phase development and evaluation of sintering temperature of prepared samples were studied by applying the TG–DTA technique. Structurally refined XRD patterns of the prepared samples revealed the phase purity and cubic spinel structure with the Fd-3m space group. The fractional atomic positions and Rietveld refinement factors were estimated from Rietveld refined XRD pattern, and also, other variations of structural parameters with zinc substitution have been calculated from XRD data. Both the Rietveld refinement and W–H method were employed to calculate the crystallite size, and both of them presented the same calculated result. The variation in the shape of particles and average particle size with Zn^{2+} substitution in Co-ferrite was evaluated from the FE-SEM technique. The formation of cubic spinel structure and change in the modes of vibrations with respect to Zn concentration in Co-ferrite of all samples were observed from the best peak-fitted Raman spectra. All the magnetic properties decreased with increasing concentration of zinc investigated from M–H loops which were obtained with the application of the VSM technique. ZFC–FC curve reveals that the blocking temperature of Co-ferrite samples decreases with increasing Zn concentration. It is possible to modulate or adjust the magnetic properties of Co-ferrite nanoparticles by Zn^{2+} doping as a favorable material for biomedical applications such as drug delivery, magnetic hyperthermia and magnetic resonance imaging (MRI).

1 Introduction

Over the past decades, significant changes have been observed in the preparation of nanoscale materials having different sizes, shapes and compositions depending on their applicability in various fields [1]. The nanoscaled materials have exceptional electric, magnetic and physical properties than their bulk appearance of the same materials [2, 3]. The nanomaterials have a prominent place in the field of research due to their essential features such as surface-to-volume ratio, dominancy of quantum effects, chemical stability and tuning feasibility [4]. Among various nanomaterials, magnetic nanomaterials (MNs) have significant applicability in a range of areas because of their excellent magnetic and electrical properties. In recent years, MNs have become promising candidates in the research field based on their novel applications such as biomedical [5], photocatalysis [6], memory storage [7], gas sensor [8] and magnetic sensor [9].

In the group of MNs, ferrites nanoparticles (NPs) are the chief materials considering their unique properties. The nanoferrites (NFs) are simply the combination of Fe_2O_3 and metallic ions (Zn, Co, Ni, Mg, Mn, Ba, Y, etc.). Based on the structure, ferrites are grouped into three types: spinel ferrite (SPF) having the general formula MFe_2O_4 (M = Zn, Co, Ni etc.); garnet ferrites (GAFs) having the general formula MFe_5O_{12} (M = Y, Eu, Cd, Dy, etc.); and hexagonal ferrite (HEF) with the general formula $MFe_{12}O_{19}$ (M = Ca, Er, Tm, etc.) [10]. Among them, SPF is the simplest form of ferrite and has excellent chemical stability, which signifies its most application in the biomedical field. The distribution of cations at the tetrahedral or octahedral site decides the normal or inverse or mixed behavior of spinel ferrite [11]. $ZnFe_2O_4$ is the example of a normal spinel structure (i.e. Zn ions accommodate only A-site), while $CoFe_2O_4$ is the example of inverse spinel (i.e., Co ions accommodate only B-site). The synthesis parameters such as the molar proportion of chemicals, pH of solution and temperature affected the properties of spinel ferrite, resulting in the change in structure that occurred [12]. Different synthesis techniques such as sol–gel, co-precipitation and thermal decomposition are employed in order to prepare SPF NPs to achieve the required biocompatibility, shape, chemical composition, size, etc., of NPs [13, 14]. Sonia et al. have investigated the synthesis

techniques affected on magnetic and structural properties of Co-ferrite NPs and found that the co-precipitation technique is the master way to produce the desired size of nanoparticles [15]. This technique is cost-effective [16], easy to do [17] and does not require any organic fuel into synthesis [18] due to these advantages, and this is a broadly used method for the preparation of SPF NPs.

Since the past decades, the study of cobalt ferrite NPs has been vastly increased with the aim to improve their properties and applications in different areas considering their higher stability, reasonable saturation magnetization, magnetostrictive coefficient and high coercivity [19]. For various applications in new technological areas such as drug delivery, antibacterial activity, magnetic hyperthermia and microwave device, the cobalt ferrite NPs act as very promising MNs due to their enhanced magnetic properties [20,21,22]. $CoFe_2O_4$ has an inverse spinel structure with Co^{2+} ions placed at B-site and Fe^{3+} ions equally distributed between A-site and B-site based on cation distribution at tetrahedral (A) site and octahedral (B) site. $ZnFe_2O_4$ has a normal spinel structure with Zn^{2+} ions predominantly placed at A-site and Fe^{3+} at B-site. The substitution of diamagnetic Zn^{2+} ions in $CoFe_2O_4$ brings about a positive change in its magnetic and structural properties [23]. When the substituted Zn^{2+} in Co-ferrite replaces Co^{2+}, Zn^{2+} A-site and Fe^{3+} ions are displaced to the B-site. In other words, most of Co preferred B-site and most of Zn preferred A-site and Fe preferred both of them. On the other hand, diamagnetic zinc substitution in hard magnetic Co-ferrite reduces magnetization [24], which approaches toward the superparamagnetic nature, which is an essential characteristic feature of NPs for biomedical applications such as the treatment of magnetic hyperthermia cancer [25]. In this regard, some researchers have presented reports on their investigation of zinc-doped mixed ferrite NPs. Ben Ali et al. have investigated the effect of Zn^{2+} doping on the magnetic and structural properties of Co–Zn ferrite NPs and found that magnetization increases with respect to zinc doping [26]. Harpreet Kaur et al. prepared Zn- and Cd-substituted cobalt ferrite by sol–gel auto-combustion method and reported that the properties of cobalt ferrite change with substitution [27]. B. Jansi Rani et al. have synthesized pure and cobalt-substituted zinc ferrite nanoparticles through a less toxic co-precipitation method and concluded that the incorporation of transition elements in the spinel ferrite structure has significant influence on the chemical, optical and structural properties of the spinel ferrite NPs [28]. K. Anu et al. synthesized $Zn_xCo_{1-x}Fe_2O_4$ water-based nanofluids and reported the effect of zinc concentration on the magnetic and structural

properties of cobalt ferrite [29]. Raghvendra et al. have synthesized Zn^{2+}-substituted Co-ferrite NPs with the application of sol–gel auto-combustion method and further ball milling and found that the Co–Zn ferrite sample with Zn^{2+} and Co^{2+} ions having equal amount showed enhanced magnetic properties [30]. According to the literature of the last decades, the Co–Zn ferrites have high stability, good saturation magnetization, low coercivity, less toxicity and excellent reusability [31,32,33]. The samples which have low coercivity and higher saturation magnetization are promising candidates for biomedical applications [31, 34, 35].

Hence, the present paper focuses on the preparation of Zn^{2+}-substituted Co-ferrite NPs, i.e., $Co_{1-x}Zn_xFe_2O_4$ (x = 0, 0.5 and 1) by a co-precipitation route, and the thermal, structural, morphological and magnetic properties of NPs were also studied by standard characterization tools. The Co–Zn ferrites have been selected for the present research because of their high sensitivity of magnetization which is a crucial factor for their applicability in biomedical field. The structural parameter and phase formation were determined using Rietveld analysis. The prepared samples possess low crystallite size and superparamagnetic behavior which is the characteristic feature of their application in the biomedical field, especially for magnetic hyperthermia.

2 Experimental

2.1 Materials and methods

The co-precipitation method was adopted to prepare $Co_{1x}Zn_xFe_2O_4$ (x = 0.0 to 1.0 in the step of 0.5). Raw materials used to synthesize zinc-doped cobalt ferrite NPs were cobalt chloride hexahydrate ($CoCl_2.6H_2O$), zinc chloride ($ZnCl_2$), ferric chloride ($FeCl_3$) and sodium hydroxide (NaOH), which was used for maintaining the pH of the solution. All chemicals utilized for synthesis were procured from Molychem PVT Limited and were AR grade. According to the chemical reaction shown in Fig. 1, NPs were prepared by co-precipitating aqueous solution of $CoCl_2.6H_2O$, $ZnCl_2$ and $FeCl_3$. In the chemical reaction, chlorides were used as raw materials; the intermediate stages were involved in the preparation of cobalt ferrite. After constant heating and stirring, nanocrystalline cobalt ferrite was obtained with some by-products such as NaCl and H_2O. Those particles were washed several times with hot distilled water to remove NaCl. The reaction shown in Fig. 1 is for $CoFe_2O_4$ (denoted as DCZ1), and the similar process

was performed for the remaining two, i.e., $Co_{0.5}Zn_{0.5}Fe_2O_4$ (denoted as DCZ3) and $ZnFe_2O_4$ (denoted as DCZ5).

Fig. 1

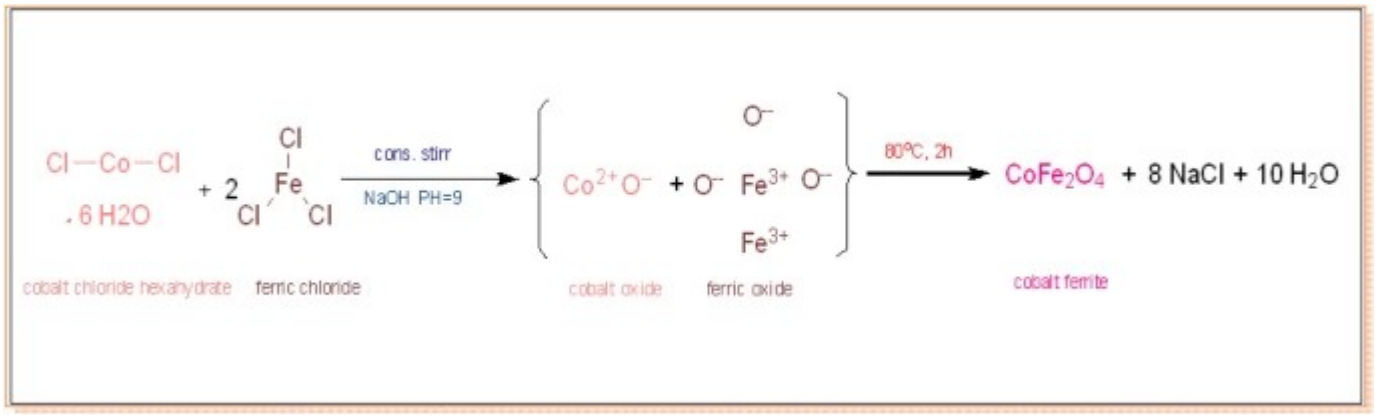

Chemical reaction of DCZ1 NPs synthesized by co-precipitation method

Initially, 50 ml of 1M (dissolved an amount of substance equal to its molecular weight in 1000 ml of distilled water) $CoCl_2.6H_2O$ and 50 ml of 2M (the double amount of its molecular weight of substance dissolved in 1000 ml of distilled water) $FeCl_3$ solutions were mixed at 300 K with steady stirring for half an hour. After complete desolation, 1M NaOH was added dropwise in the mixed solutions to regulate the pH value at nine. Then, the obtained solution was heated at 80 °C with constant stirring at 300 rpm for 2 h. After the processes were completed, the solution was left to cool down to room temperature under stirring conditions. Further, the precipitates were again washed with the distilled water several times. Then, washed particles were separated from water with the help of the centrifugal separator. The NPs were dehydrated at 300 K for 48 h. The prepared powder of NPs was ground for 50 min, and after thermal analysis, it was sintered at 900 °C for 4 h. A similar synthesis process was done forDCZ3 and DCZ5 samples. The sintered powder of all samples was used for the structural, morphological and magnetic characterization.

2.2 Characterizations

The as-prepared powder of the sample was characterized by ‘thermogravimetric and

differential thermal analysis' (Shimadzu DTA-60H) to evaluate the thermal properties and also to confirm sintering temperature. Rietveld refinement of 'X-ray diffraction (XRD)' (Bruker) patterns was carried out by using the FullProf Suit program, and Rietveld refinement was performed with the help of Pseudo-Voigt function. Crystallite size was calculated by applying Rietveld refinement as well as the Williamson–Hall plot. The surface morphological investigation of prepared samples was performed by using the 'field emission scanning electron microscopy (FE-SEM)' (SUPRA 55FE-SEM) technique. Raman spectra of samples were recorded with the help of Raman spectroscopy (Jobin Yvon Horiba LABRAM-HR 800) at room temperature within the frequency range of 200–800 cm^{-1}. The peak fitting of Raman spectra was carried out by Origin Pro 8.6 software applying the Lorentzian function. Using a 'vibrating sample magnetometer (VSM)' (Quantum Design-Modular control system) at room temperature with an applied magnetic field ± 30kOe, the magnetic properties of samples were investigated. Field-cooled (FC) and zero-field-cooled (ZFC) curves of all samples were carried out under the 500Oe applied magnetic field and between the temperature range of 0 K and 350 K (Fig. 2).

Fig. 2

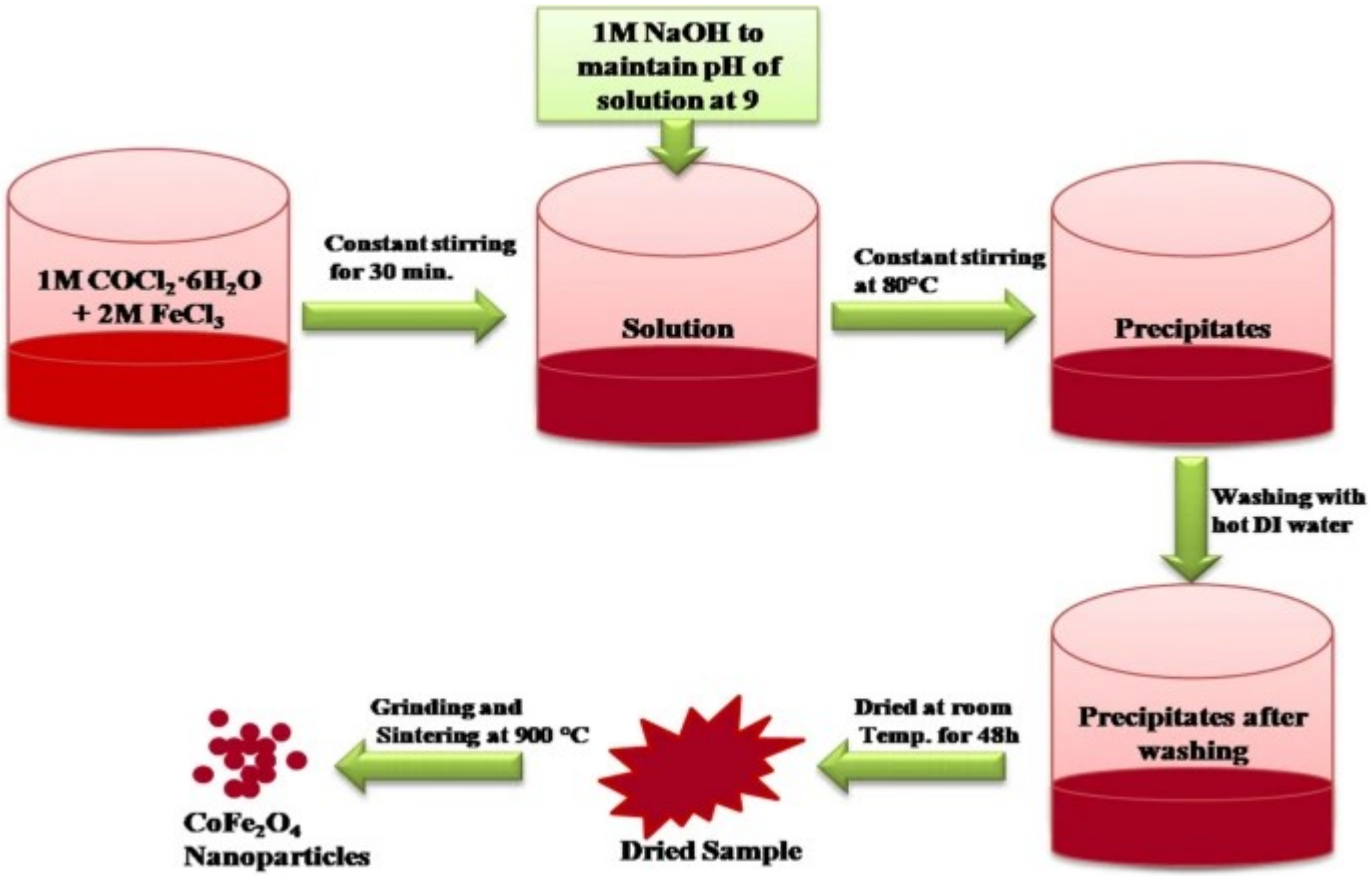

Schematic version of a co-precipitation synthesis route for the preparation of DCZ1 NPs

3 Results and discussion

3.1 Thermal studies

The thermal analysis was performed for understanding the decomposition of metal hydroxide, removal of water and ferritization temperature of the prepared samples under a nitrogen atmosphere and in the temperature range of 27 °C to 1000 °C with 20 °C/min heat step. The TG–DTA curve of DCZ1 sample is shown in Fig. 3. From TG–DTA analysis, it is clear that those three different events of weight loss exhibit in the TGA curves which have corresponding endothermic and exothermic peaks observed in the DTA curve. The initial loss in weight was observed to be 8.5% in the temperature range between 27 °C and 355 °C, which arises due to the removal of moisture, and there is no corresponding endothermic peak observed in the DTA analysis. The second weight loss of 18.81% was observed in the temperature range of 355–416 °C which corresponds to exothermic peak at 400 °C of the DTA curve, which indicates the disintegration of metallic hydroxides. Further, the third weight loss of 5.71% and endothermic peak at 549.6 °C show ferritization temperature of ferrite. The total loss in the weight of DCZ1 sample (i.e., 33.02%) was completed up to the 886 °C. Thus, all the prepared samples were sintered at 900 °C for 4 h.

Fig. 3

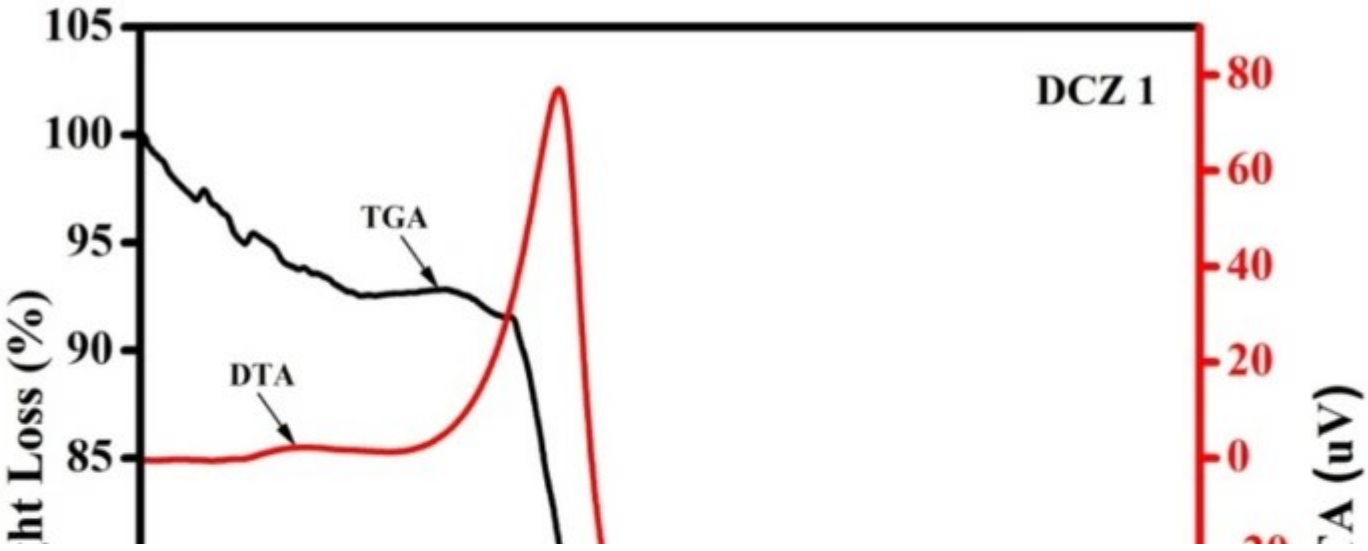

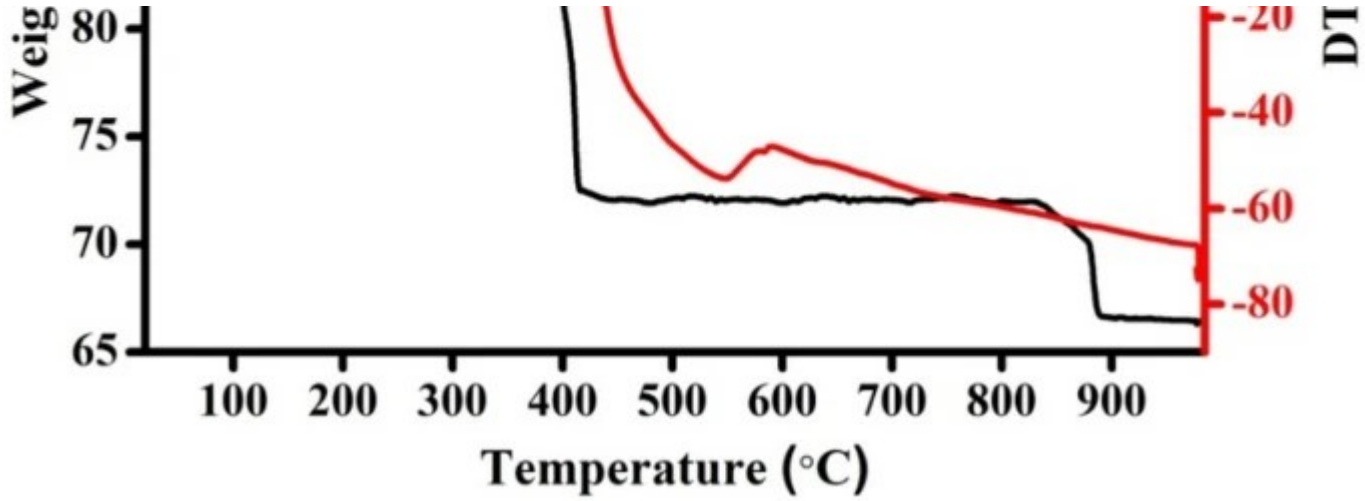

TG–DTA curve of DCZ1

3.2 Structural properties

Rietveld refinement pattern of XRD data of DCZ1, DCZ3 and DCZ5 is shown in Fig. 4, which was performed using FullProf Suit. In Fig. 4, red-colored points signify the experimentally observed data and the black-colored line denotes the calculated intensity. Vertical lines represent Bragg's positions which are allowed for the Fd-3m space group (Fig. 5). The blue-colored line at the bottom represents the difference between calculated and measured intensity levels. Refinements in XRD patterns by Rietveld revealed the phase identification of samples. The quality of refinement was evaluated by using the reliability factors in Rietveld refinement [36, 37]. The Rietveld refinement factors such as χ^2, R_p, R_{wp} and R_{exp} of prepared samples are shown in Table 1. The χ^2 values of all samples are observed to be closer to 1, which implies an almost good quality of fit. The values of lattice parameters 'a_{rt}' concluded from Rietveld refinement and 'a' of all samples calculated from Eq. 1 are given in Table 4.

$$\sin^{2} \theta = \left({\lambda^{2} /a^{2} } \right)\left({h^{2} + k^{2} + l^{2} } \right)$$

(1)

Fig. 4

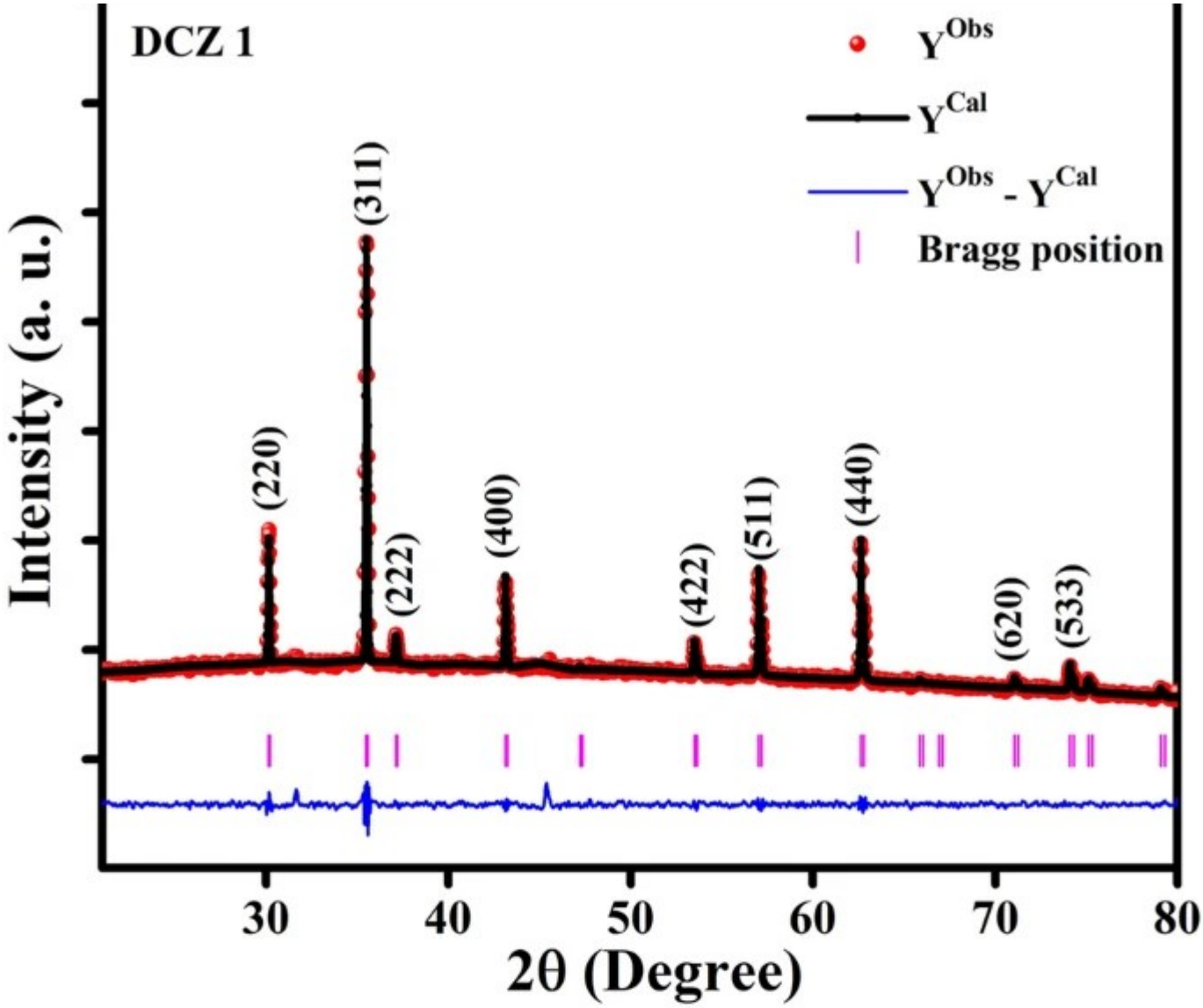
DCZ 1
Y^{Obs}
Y^{Cal}
$Y^{Obs} - Y^{Cal}$
Bragg position
Intensity (a. u.)
(220)
(311)
(222)
(400)
(422)
(511)
(440)
(620)
(533)
30
40
50
60
70
80
2θ (Degree)

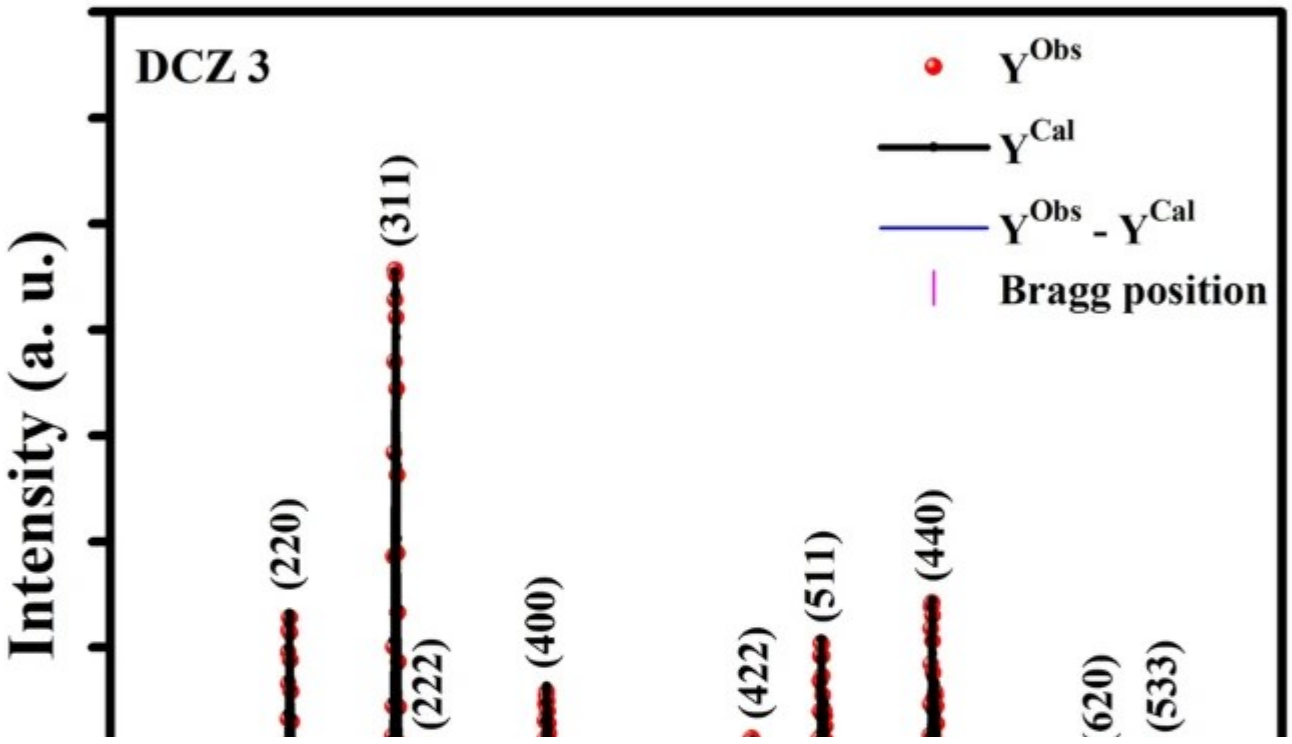
DCZ 3
Y^{Obs}
Y^{Cal}
$Y^{Obs} - Y^{Cal}$
Bragg position
Intensity (a. u.)
(220)
(311)
(222)
(400)
(422)
(511)
(440)
(620)
(533)

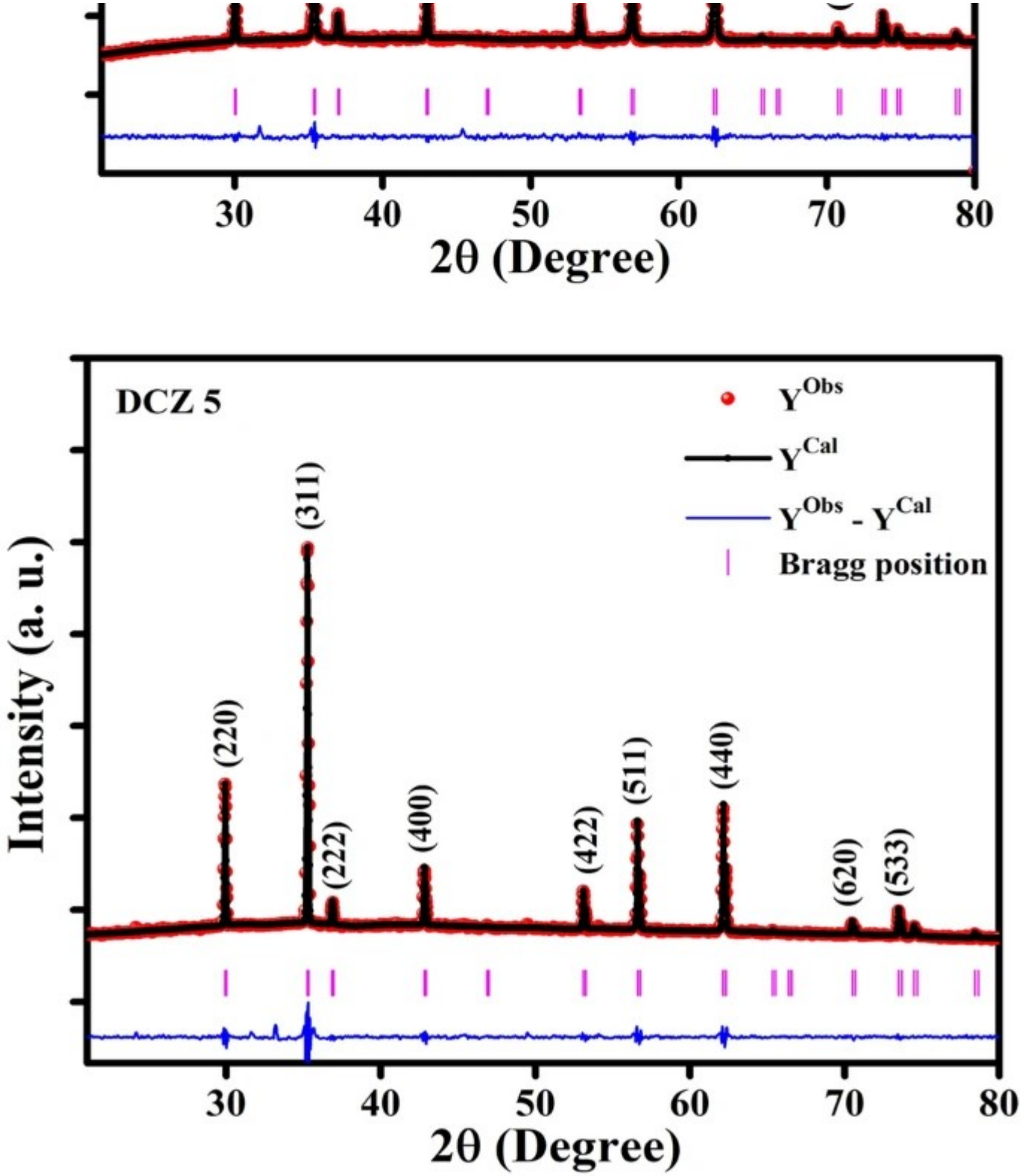

Rietveld refined XRD pattern for DCZ1, DCZ3 and DCZ5

Fig. 5

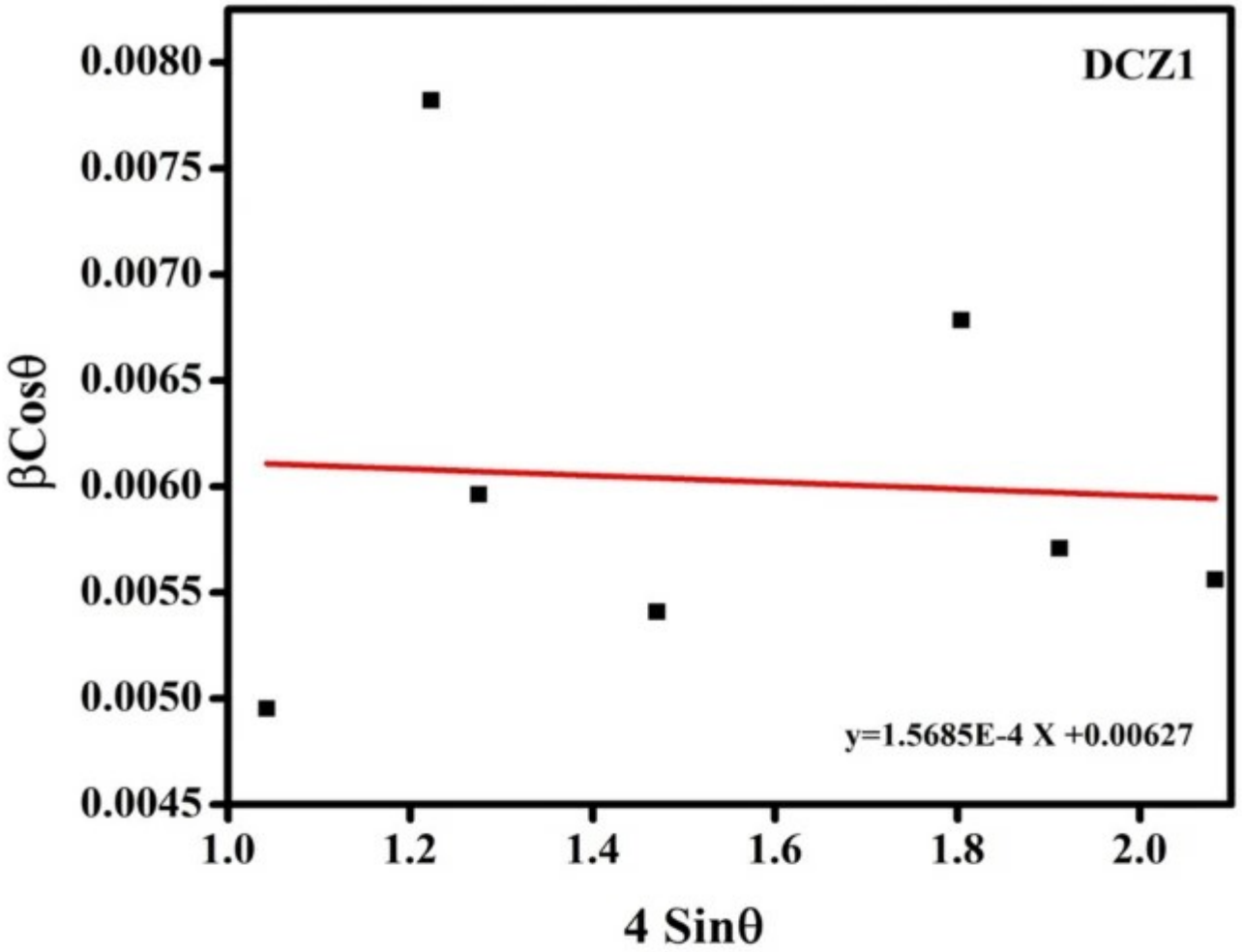
DCZ1
0.0080
0.0075
0.0070
0.0065
0.0060
0.0055
0.0050
0.0045
βCosθ
y=1.5685E-4 X +0.00627
1.0
1.2
1.4
1.6
1.8
2.0
4 Sinθ

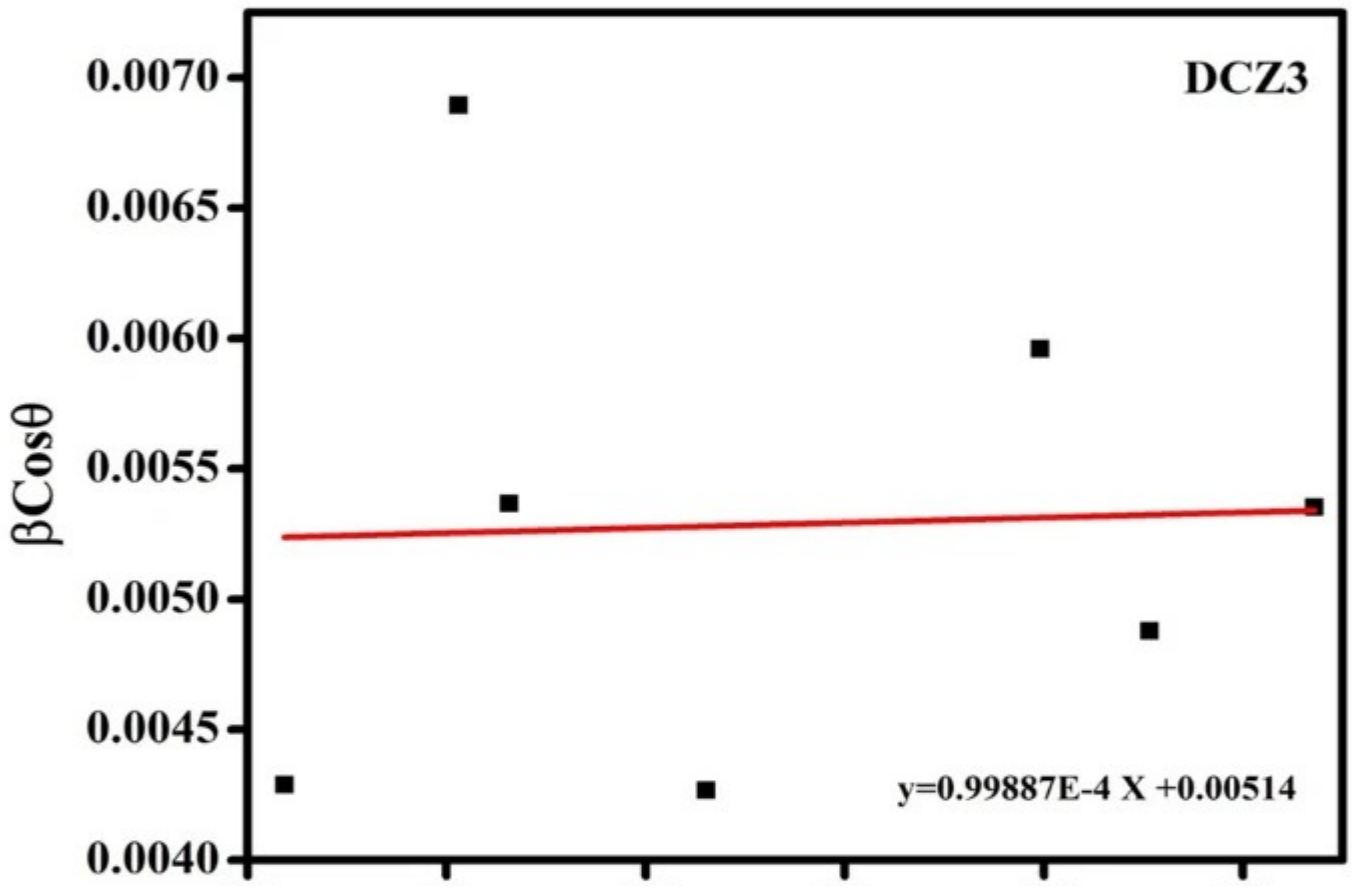
DCZ3
0.0070
0.0065
0.0060
0.0055
0.0050
0.0045
0.0040
βCosθ
y=0.99887E-4 X +0.00514

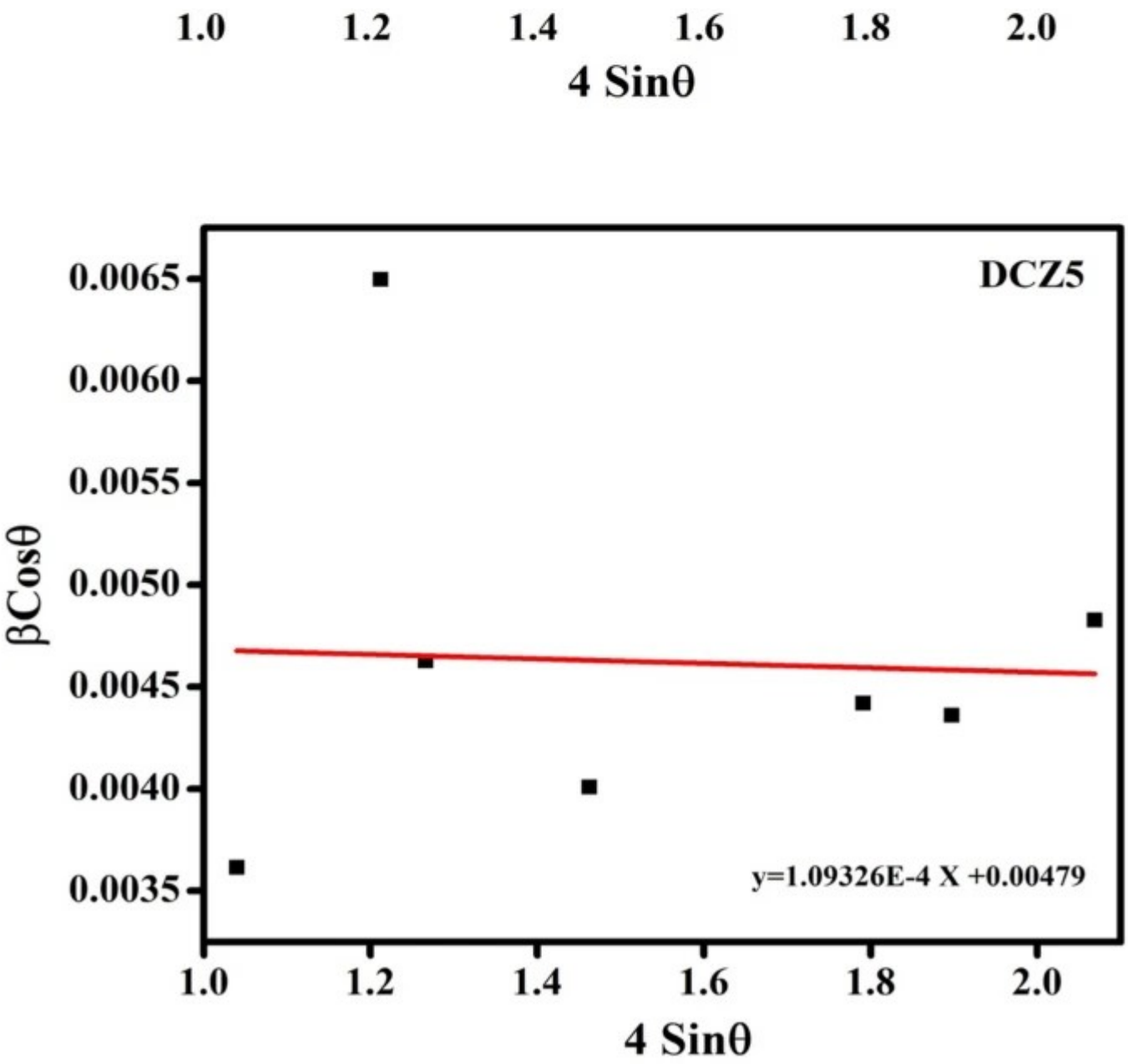

Williamson–Hall plot of DCZ1, DCZ3 and DCZ5

Table 1 Rietveld refinement factors: profile factor (R_p), weighted profile factor (R_{wp}) and expected R-factor (R_{exp}) of DCZ1, DCZ3 and DCZ5 samples

where h, k and l are the Miller indices of the plane, θ is the Bragg's angle, a is the lattice

constant and λ is the X-ray wavelength. With increasing zinc concentration, the values of 'a_{rt}' and 'a' are found to be similar and increased. The calculated standard deviation of 'a_{Rt}' and 'a' (SD) is given in Table 4, which is found very small for each sample. The low standard deviation indicates the data are clustered around the mean, which proves calculated values from both methods are much closed to each other. The graphical representation of the values of 'a_{rt}' and 'a' of all samples is shown in Fig. 6a. Perhaps, due to the difference in the ionic radii of Co^{2+} (0.72 Å) and Zn^{2+} (0.74 Å) ions, a change in the value of the lattice parameter was observed with increasing zinc concentration.

Fig. 6

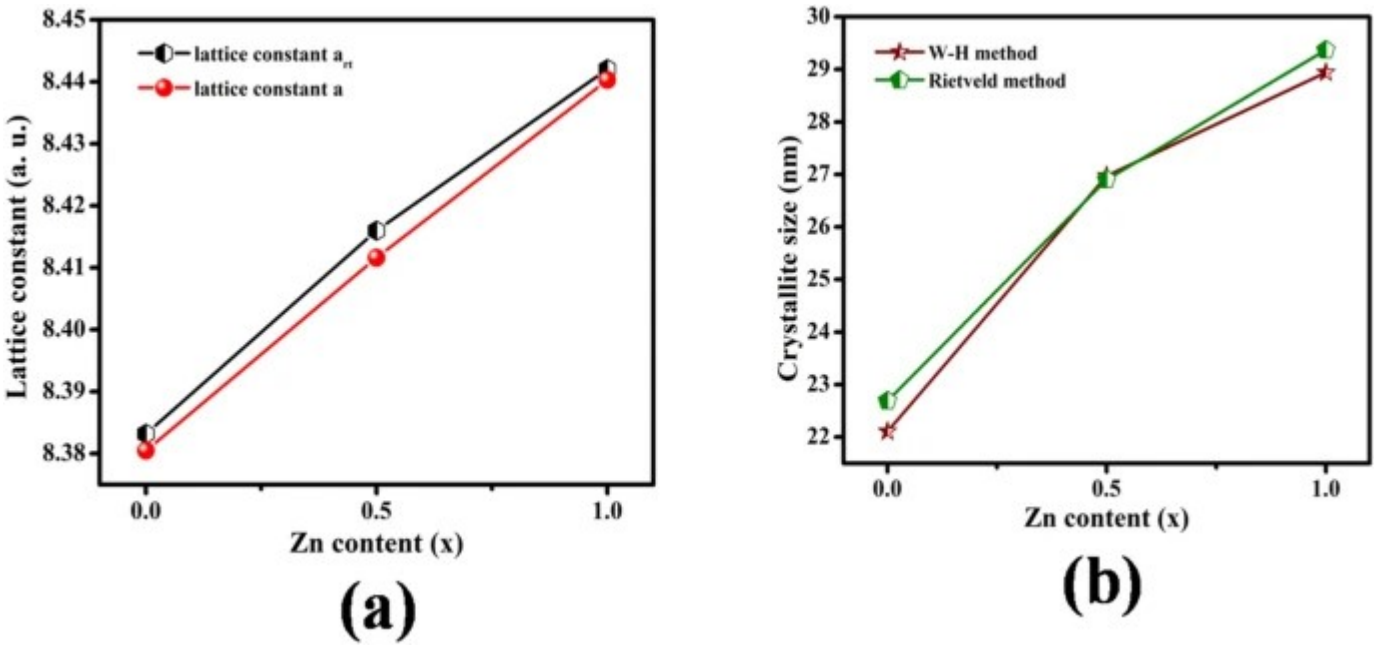

a Variation of calculated (a) and concluded from Rietveld refinement (a_{rt}) lattice constant; b variation of crystallite size calculated from W–H method and Rietveld method for samples DCZ1, DCZ3 and DCZ5

The Wyckoff positions and x, y and z coordinates of respective atoms used in refinement are shown in Table 2. In the case of all the three refined samples, slit variation was seen in the Wyckoff position of 32e, whereas 8a and 16d did not show any variation in its x, y and z coordinates. The structural parameters L_A, L_B, d_{BL}, d_{AL}, d_{BL}, d_{AE}, d_{AE} and ionic radii (r_A and r_B) were determined with the help of the values of lattice constant 'a' and oxygen positional

parameter 'u' having the standard value 0.0375 nm. The hopping lengths for A-site (L_A) and B-site (L_B) were calculated using standard Eqs. 2 and 3, respectively [38]. Octahedral bond length (d_{BL}), tetrahedral bond length (d_{AL}), tetra edge (d_{AE}) and octa edge (d_{BEU}) shared and unshared values were evaluated applying Eqs. 4, 5, 6, 7 and 8, respectively [39]. The calculated values of structural parameters of all samples are given in Table 3. The values of all parameters except L_A and L_B have been enhanced with increasing concentration of zinc.

$$L_{A} = a\sqrt {3/4} \;{{\AA}}$$

(2)

$$L_{B } = a\sqrt {2/4} \;{{\AA}}$$

(3)

$$d_{BL } = a\sqrt {3u^{2} - (11/4)u + (43/64)} \;{{\AA}}$$

(4)

$$d_{{{\text{AL}}}} = a\sqrt 3 (u - 1/4)\;{{\AA}}$$

(5)

$$d_{{\text{AE }}} = a\sqrt 2 \left({2u - 1/2\;{{\AA}}} \right)$$

(6)

$$d_{{{\text{BE}}}} = a\sqrt 2 \left({1 - 2u} \right)\;{{\AA}}$$

(7)

$$d_{{{\text{BEU}}}} = a\sqrt {4u^{2} - 3u + \left({11/6} \right)} \;{{\AA}}.$$

(8)

Table 2 Wyckoff positions and x, y, z coordinates of respective atoms used in Refinement

Table 3 Hopping length (L_A, L_B), ionic radii (r_A, r_B), tetrahedral bond length (d_{AL}), octahedral bond length (d_{BL}), tetra edge (d_{AE}) and octa edge shared (d_{BE}) and unshared (d_{BEu}) for the samples DCZ1, DCZ3 and DCZ5

Using the radius of oxygen anions [i.e., r(O)], the tetrahedral ionic radii (A-site) and octahedral ionic radii (B-site) were determined by Eqs. 9 and 10, respectively [40], and the calculated values of r_A and r_B are included in Table 3.

$$r_{A } = \left({u - 1/4} \right)a\sqrt 3 - r\left({O^{2 - } } \right)\;{{\AA}}$$

(9)

$$r_{B} = \left({5/8 - u} \right) - r\left({O^{2 - } } \right)\;{{\AA}}.$$

(10)

The computed values of both A-site and B-site ionic radii of all samples were observed to be increased with increasing concentration of zinc. A-site ionic radii increase from 0.5821 to 0.5955 Å, while B-site ionic radii increase from 0.7255 to 0.7399 Å with the concentration of zinc ($x = 0$, 0.5 and 1).

The modified Williamson–Hall plots of prepared samples are shown in Fig. 5, based on the uniform deformation model (UDM) (Eq. 12) [41]. The UDM considers uniform strain along with crystallographic direction, which is observed in nanocrystals due to crystal imperfections. Based on strain and size in particular peak having hkl value, the total broadening has been expressed as shown in Eq. 11.

$$\beta_{{{\text{hkl}}}} = \beta_{{{\text{size}}}} + \beta_{{{\text{strain}}}}.$$

(11)

The W–H plots are drawn with 4sinθ on the x-axis and βCosθ on the y-axis to calculate crystallite size. From the straight line, crystallite size and intrinsic strain were calculated. The crystallite size has been determined from the intercept on the y-axis [42]; the slope of straight line provides intrinsic strain, which are given in Table 4.

$$\beta \cos \theta = \frac{k\lambda }{D} + 4\varepsilon {\text{Sin}} \theta.$$

(12)

Table 4 Lattice constant inferred from Rietveld refinement (a_{Rt}), calculated lattice constant (a), standard deviation of 'a_{Rt}' and 'a' (SD), strain ε (10^{-4}) from W–H plot, crystallite size calculated by W–H method and Scherrer's formula for samples DCZ1, DCZ3 and DCZ5

All samples have positive slope which indicates the lattice expansion and hence produce an intrinsic strain in the nanocrystals.

The comparison of crystallite size of DCZ1, DCZ3 and DCZ5 samples was calculated by Scherrer's equation and Williamson–Hall plot, which is provided in Table 4. The crystallite size was calculated from Debye–Scherrer's formula with the help of FWHM of the refined XRD peaks [43].

$$D = {\raise0.7ex\hbox{${k\lambda }$} \!\mathord{\left/ {\vphantom {{k\lambda } {\left({\beta cos\theta } \right)}}} \right.\kern-\nulldelimiterspace} \!\lower0.7ex\hbox{${\left({\beta cos\theta } \right)}$}}$$

where D is the crystallite size of the particles, λ is the X-ray wavelength, k is a constant (k = 0.9), θ is the peak position of the identified crystalline phase and β is the full width at half

maximum (FWHM). The crystallite size obtained from both the ways of all samples was observed to rise with increasing zinc concentration. Kumar et al. reported the comparative study of the crystallite size of Co–Zn ferrite NPs calculated by using Scherer's, W–H and Rietveld three different methods [44]. In the present case, the crystallite size of all samples is calculated by both W–H method and Scherrer's formula. The obtained crystallite size was found same except DCZ5, because it may be the strain correction factor which has been used while using the Williamson–Hall method. The graphical representation of comparative variation in crystallite size was calculated by both of the methods shown in Fig. 6b.

3.3 FE-SEM analysis

The FE-SEM technique was used to investigate the changes that occurred in the surface morphology with zinc doping in cobalt ferrite. Figure 7 shows FE-SEM images and corresponding histogram distribution of DCZ1, DCZ3 and DCZ5 nanoparticles. These images show agglomeration between the particles, and the particles appeared nearly spherical. The average particle size of DCZ1, DCZ3 and DCZ5 samples estimated from the histograms was found to be 22 nm, 32 nm and 46 nm, respectively, which increased with the increasing zinc concentration in Co-ferrite. The obtained particle size was found to be larger than the crystallite size that was obtained from the W–H plot and Scherrer's method, which may be because some crystallites with different orientations consisted of NPs [45]. The nanocrystalline nature of the samples was confirmed by the nano ranging size of nanoparticles, which is initially confirmed by the crystallite size obtained from Rietveld analysis.

Fig. 7

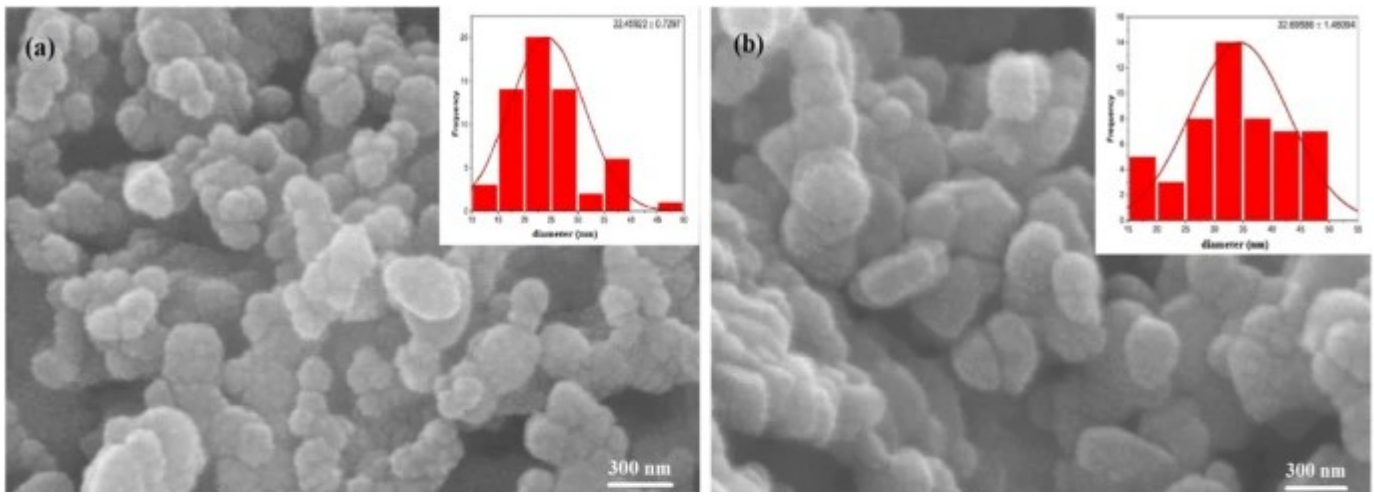

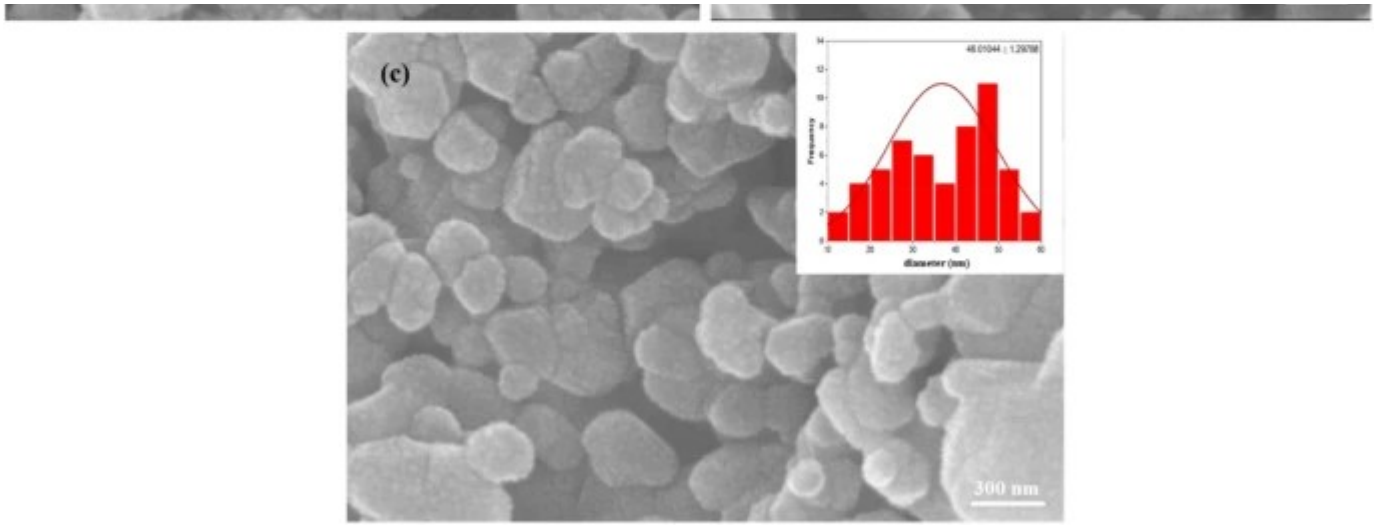

FE-SEM images and histogram of DCZ1, DCZ3 and DCZ5 NPs

3.4 Raman spectra study

Raman spectra of prepared NPs were recorded at 300 K within the frequency range of 200–800 cm^{-1}. Figure 8 displays the Raman spectra of DCZ1, DCZ3 and DCZ5 samples. Co–Zn ferrite NPs have Fd3m space group which generates 39 vibrational modes [46]. Group theory predicted that A_{1g}, E_g and $3T_{2g}$ these five modes are Raman active out of 39 modes. Three T_{2g} modes are labeled: T_{2g} (1), which is the lowest frequency mode, and T_{2g} (2) and T_{2g} (3), which are the highest frequency modes of this vibrational species [47]. A_{1g}, E_g and $3T_{2g}$ Raman active peaks were expected for the appearance of the cubic phase, which is clearly visible in all prepared samples spectra. In the case of the spinel structure, Raman active modes composed the motion of oxygen and both A-site and B-site metal ions. The parameters of Raman spectra such as the natural tendency of frequency, intensity, integrated intensity and full width at half maximum of peaks were determined by using a best-fitting procedure based on the Lorentzian function. In the case of spinel ferrite, the frequencies of Raman peaks above 600 cm^{-1} are the indication of the tetrahedral site and those below 600 cm^{-1} represent the octahedral site. The higher frequency A_{1g} mode is the presentation of symmetric stretching of metal–oxygen at tetrahedral site. In the case of cobalt ferrite, Raman spectra show A_{1g}(1) and A_{1g}(2) modes, Co and Fe ions occupied the octahedral site, whereas only Fe ion occupied the tetrahedral site. The bond distance of Fe–O and Co–O redistributed between both the sites; because Co and Fe ions have different ionic radii, the cobalt ferrite shows doublet-like structure [48]. There are also other four low-frequency phonon modes, in which E_g and

$T_{2g}(3)$ modes are attributed to the symmetric and asymmetric bending of O^{2-} to metallic ion, correspondingly. The $T_{2g}(2)$ and $T_{2g}(1)$ modes represent asymmetric stretchings and bending of O^{2-} atoms at the octahedral site, respectively. The calculated values of Raman modes are listed in Table 5. Raman spectra of DCZ1 show six peaks maxima at 193.3 cm^{-1}, 298.5 cm^{-1}, 462.1 cm^{-1}, 552.2 cm^{-1}, 605.5 cm^{-1} and 682.8 cm^{-1}. Also Raman spectra of DCZ3 and DCZ5 samples show six peaks maxima at 184.6 cm^{-1}, 312 cm^{-1}, 467.4 cm^{-1}, 544.0 cm^{-1}, 617.5 cm^{-1} and 678.6 cm^{-1} and 190.7 cm^{-1}, 296 cm^{-1}, 461.9 cm^{-1}, 550.6 cm^{-1}, 604.5 cm^{-1} and 681.0 cm^{-1}, respectively. This study revealed that the variation observed in Raman modes of three samples with respect to particle size and particle size increases with increasing Zn concentration in Co-ferrite.

Fig. 8

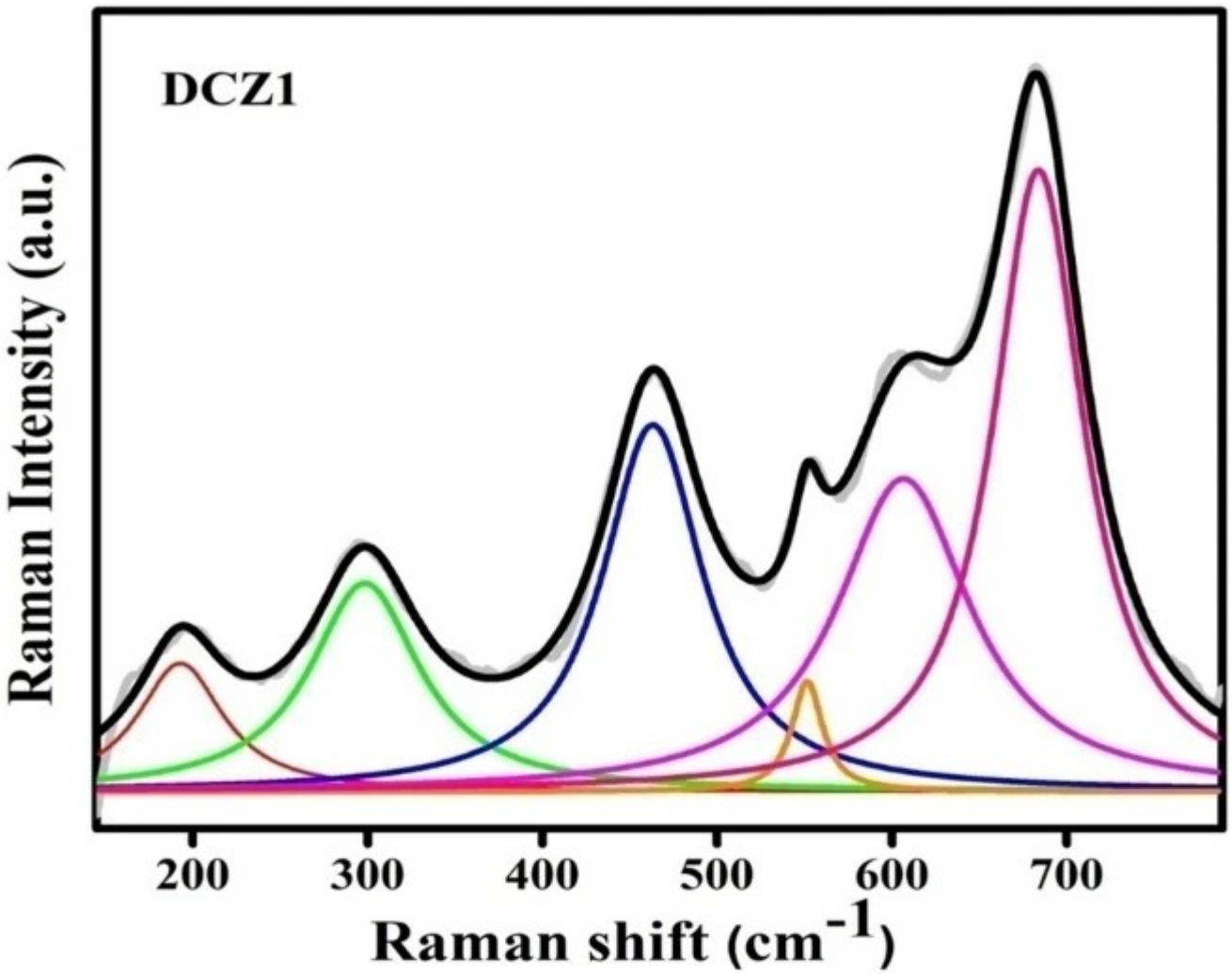

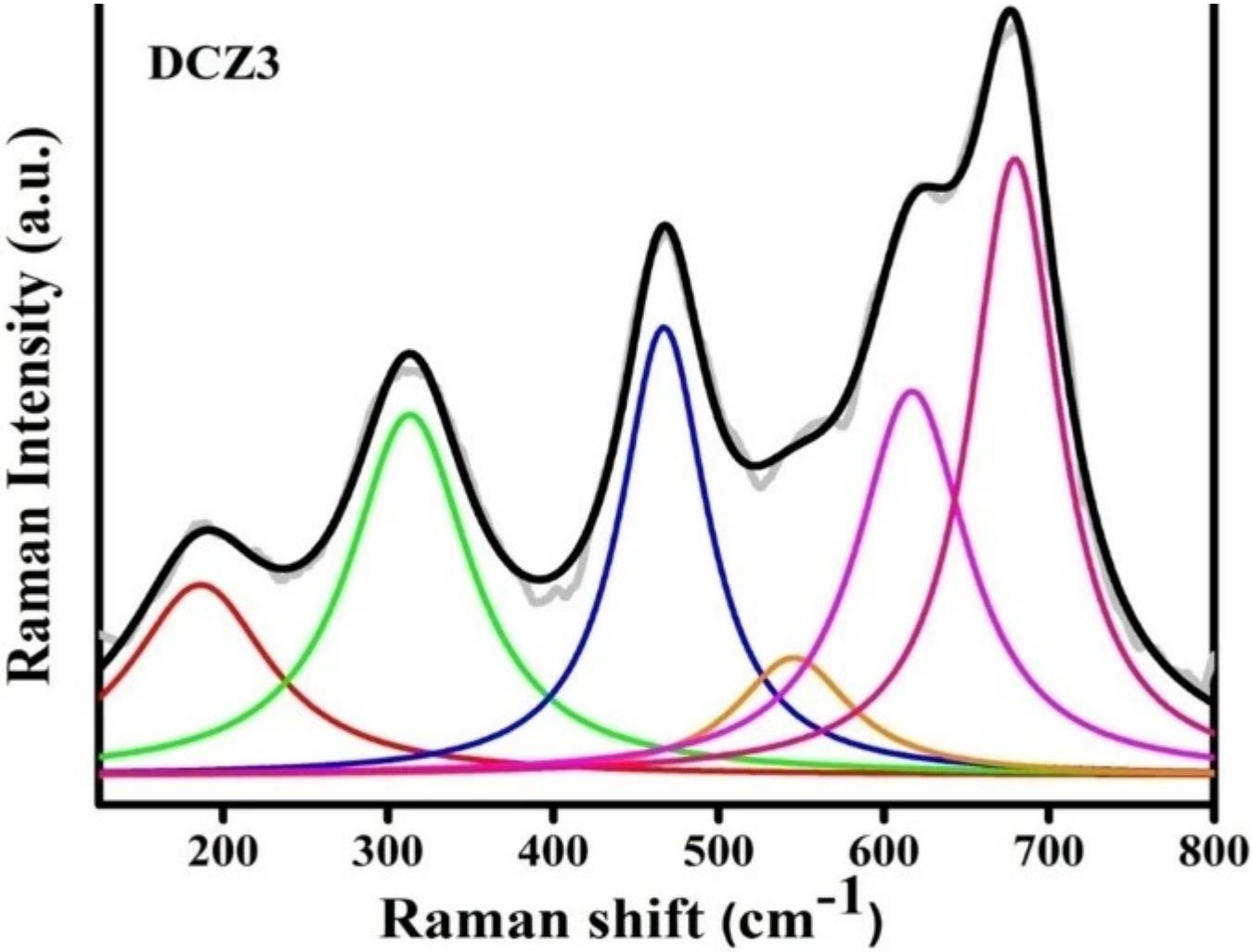
DCZ3
Raman Intensity (a.u.)
200
300
400
500
600
700
800
Raman shift (cm-1)

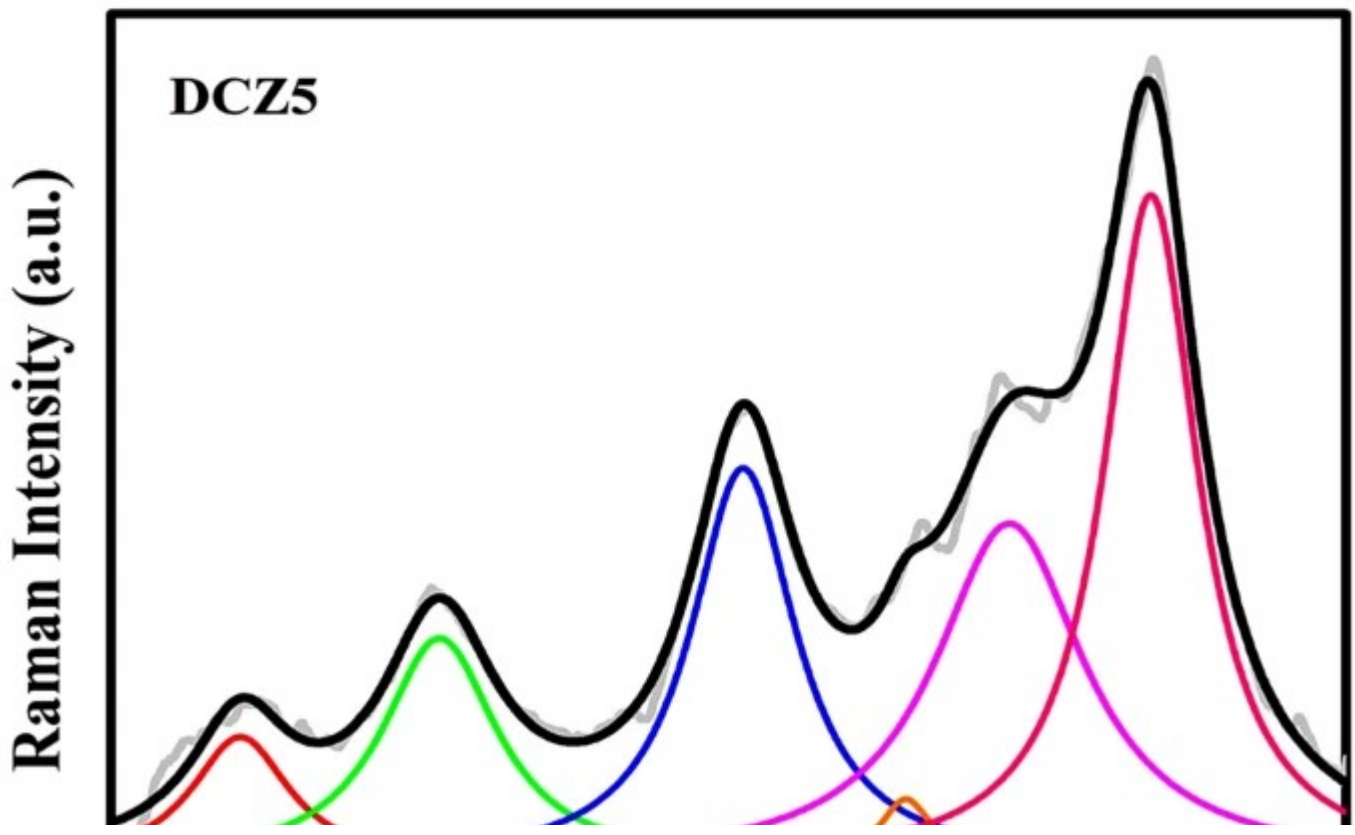
DCZ5
Raman Intensity (a.u.)

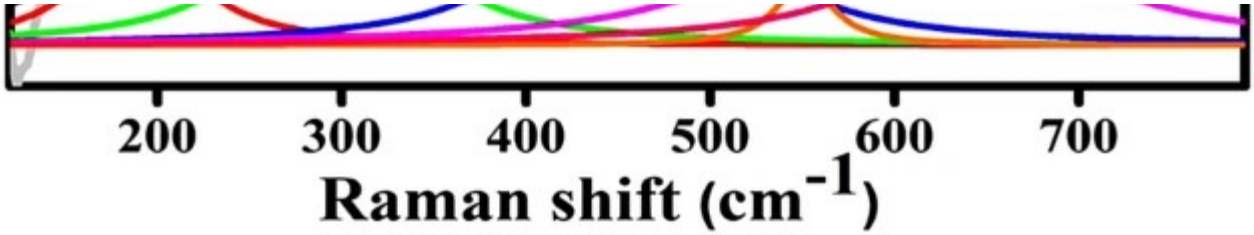

Best fitting of Raman spectra for DCZ1, DCZ3 and DCZ5 samples in the range 100–800 cm^{-1}

Table 5 Raman active modes for DCZ1, DCZ3 and DCZ5 samples

3.5 Magnetic properties

3.5.1 M–H analysis

The prepared NPs were investigated by the VSM technique at 300 K to evaluate their magnetic properties. The M–H plots of samples DCZ1, DCZ3 and DCZ5 are recorded with an applied magnetic field of 30000Oe to 30000Oe at 300 K as shown in Fig. 9. Cobalt ferrite shows hard magnetic behavior with high saturation magnetization and coercivity as compared to zinc ferrite [49]. The results of M–H loops revealed that DCZ1 had a broader loop as compared to the loops formed due to zinc substitution and pure zinc ferrite (i.e., DCZ3 and DCZ5 samples). The observed saturation magnetization (M_s) of DCZ1, DCZ3 and DCZ5 was 59.25 emu/g, 42.32 emu/g and 4.52 emu/g, respectively, showing the decreasing order. Also the calculated value of coercivity of DCZ1, DCZ3 and DCZ5 samples was 501.37Oe, 279.32Oe and 16.67Oe, correspondingly. The M_S and H_C values of samples decrease with the increasing concentration of zinc because of exchanging A–B interaction, the detailed description of which was reported in our previous research paper [50]. The remanence magnetization (M_r) value of DCZ5 was fined nearly zero (i.e., 0.025 emu/g), which may be due to the nonmagnetic nature of zinc. The M_r value of DCZ1 and DCZ3 samples is 18.24 emu/g and 11.02 emu/g, respectively. The magneton number of prepared NPs was calculated using Eq. 12.

$$n_{B} = \left[{M_{s} \times M_{w} } \right]/5585.$$

(13)

Fig. 9

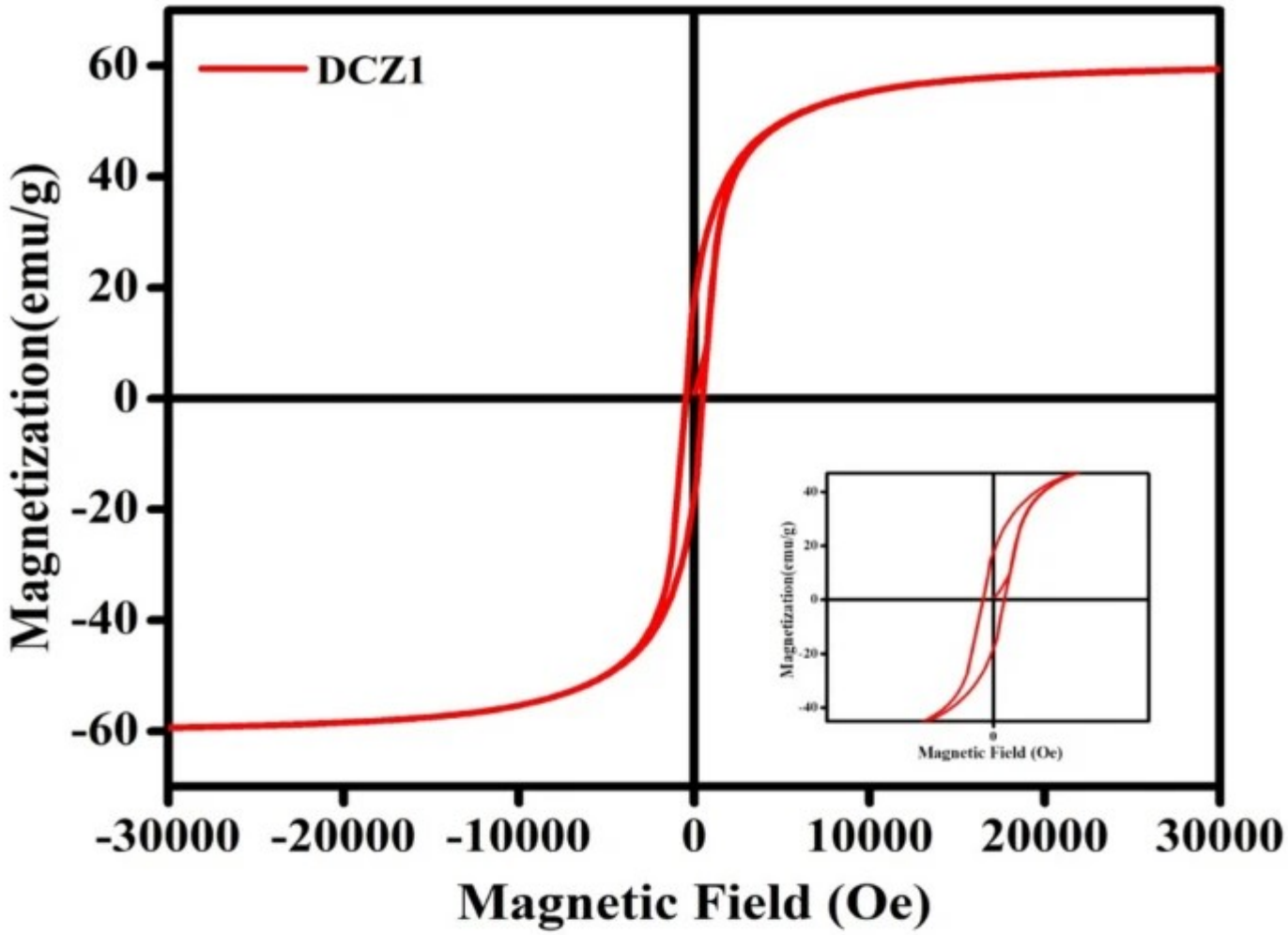
DCZ1
Magnetization(emu/g)
60
40
20
0
-20
-40
-60
-30000
-20000
-10000
0
10000
20000
30000
Magnetic Field (Oe)
Magnetization(emu/g)
Magnetic Field (Oe)

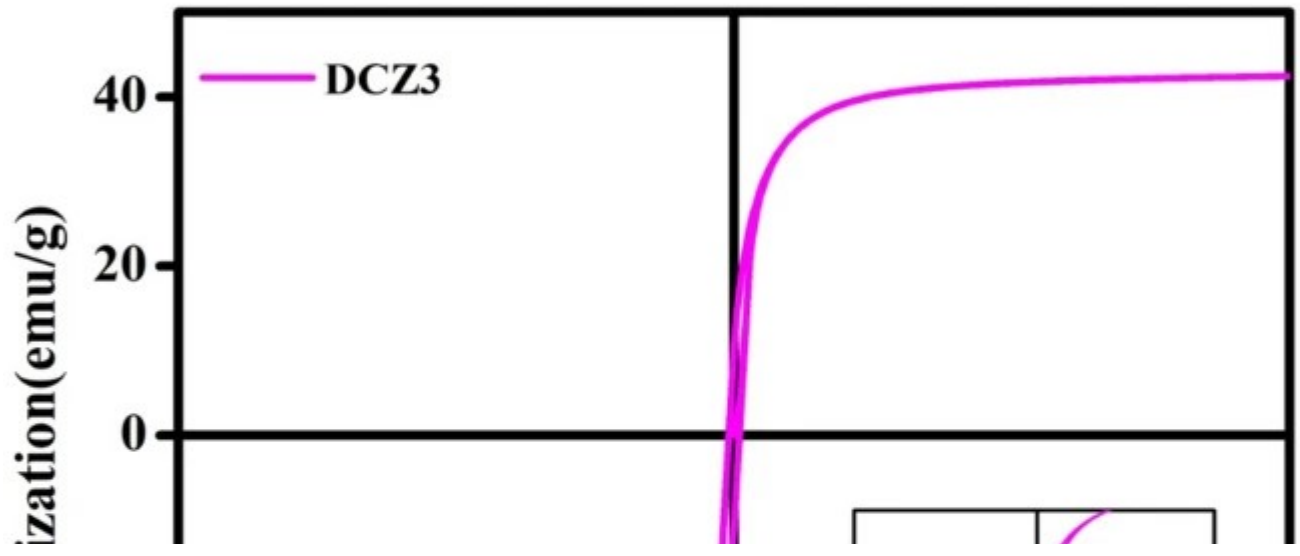
DCZ3
40
20
0

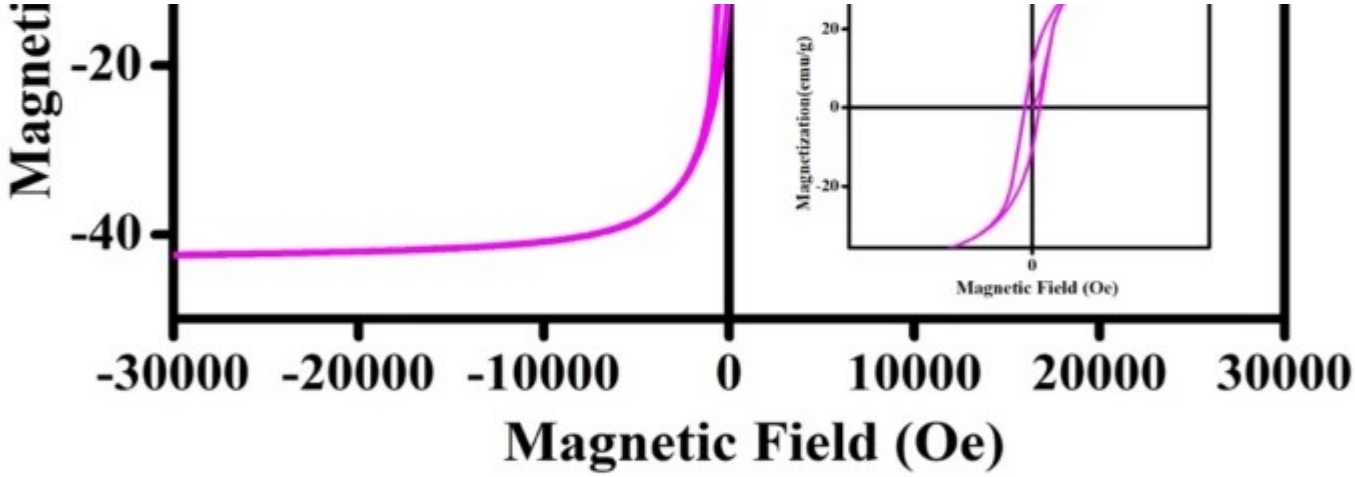

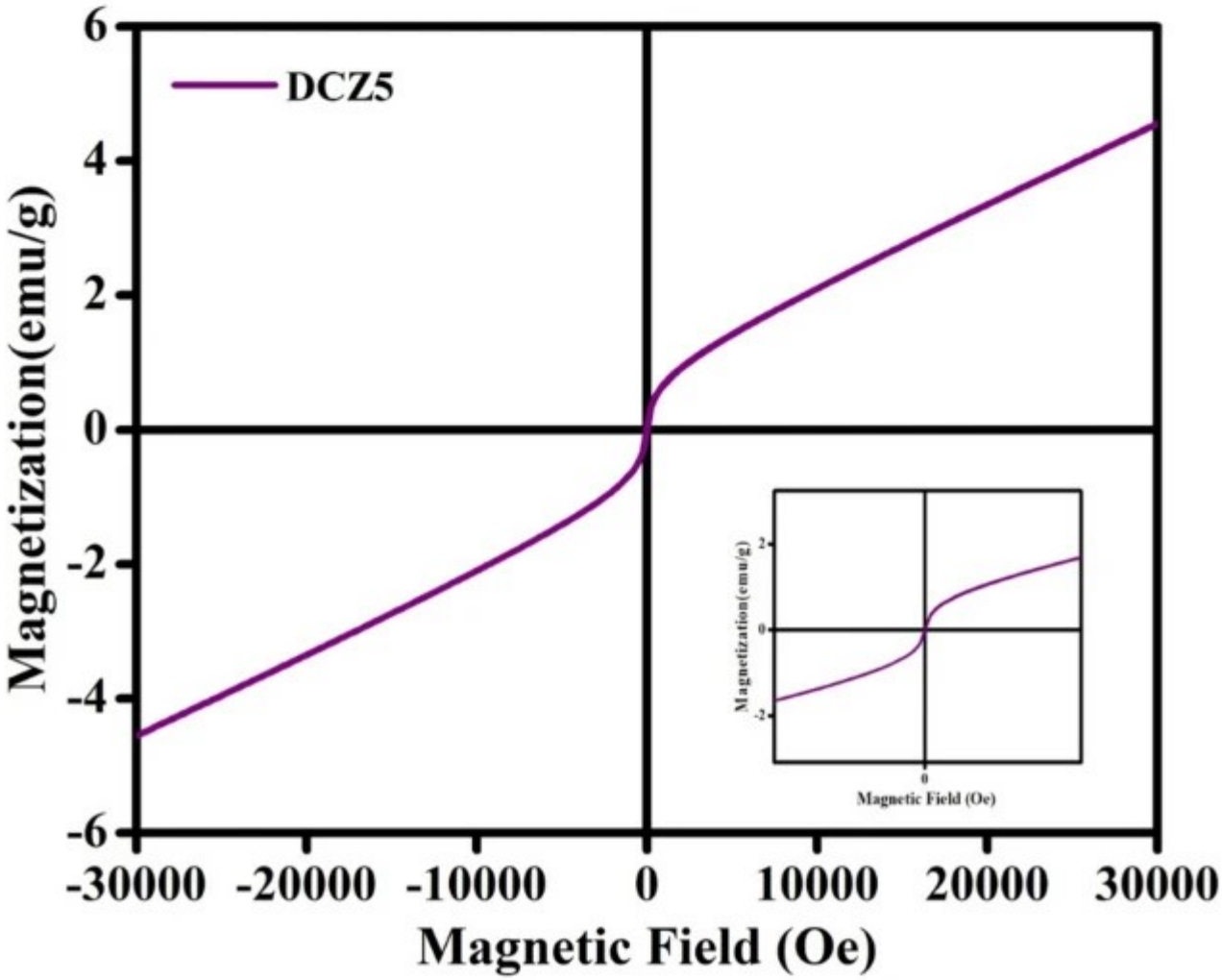

Room-temperature magnetic hysteresis loop of samples DCZ1, DCZ3 and DCZ5

The calculated n_B value of DCZ1, DCZ3 and DCZ5 samples is 2.48 μ_B, 1.80 μ_B and 0.19 μ_B,

respectively. The estimated magnetic parameters of NPs are given in Table 6. The value of H_c and M_r approaches to zero, which is the typical feature of the superparamagnetic behavior of magnetic NPs as reported by Aravind et al. [51]. The NPs having superparamagnetic nature are the essential condition for their applicability in the biomedical field (such as magnetic hyperthermia and drug delivery). From the VSM analysis, it is clear that prepared NPs possess superparamagnetic behavior at room temperature and these nanoparticles are very useful for biomedical applications.

Table 6 Magnetic parameters values of the saturation magnetization (M_s), coercivity (H_c), remanence magnetization (M_r), remanence ratio (M_r/M_s), magneton number (n_B) and blocking temperature (T_B) calculated from M−H loop and ZFC−FC curves of DCZ1, DCZ3 and DCZ5 samples

3.5.2 M−T analysis

Field-cooled (FC) and zero-field-cooled (ZFC) plots of DCZ1, DCZ3 and DCZ5 NPs were measured under applied magnetic field 500Oe and between the temperature range of 0K and 350 K as shown in Fig. 10. The ZFC curve was recorded in two steps: First, without the presence of exterior magnetic field, nanoparticles were cooled down, and then, under 500Oe external applied magnetic fields, the magnetization (MZFC) of NPs was recorded during the increase of temperature from 0 to 350 K. Later, in the presence of 500 Oe applied magnetic field samples were cooled down, after that recorded magnetization (MFC) of nanoparticles during heating up to 350 K. The evaluation of the magnetic performance of the sample from FC-ZFC curve can be easily explained with the help of two physical properties such as blocking temperature and irreversibility temperature. The ZFC measurement results reveal that in the initial stage, with increasing temperature, magnetization also increases. The specific temperature at which magnetization reaches its maximum value is known as blocking temperature (T_B), whereas the temperature at which FC and ZFC curves split from each other is called irreversibility temperature (T_{irr}) [52, 53].

Fig. 10

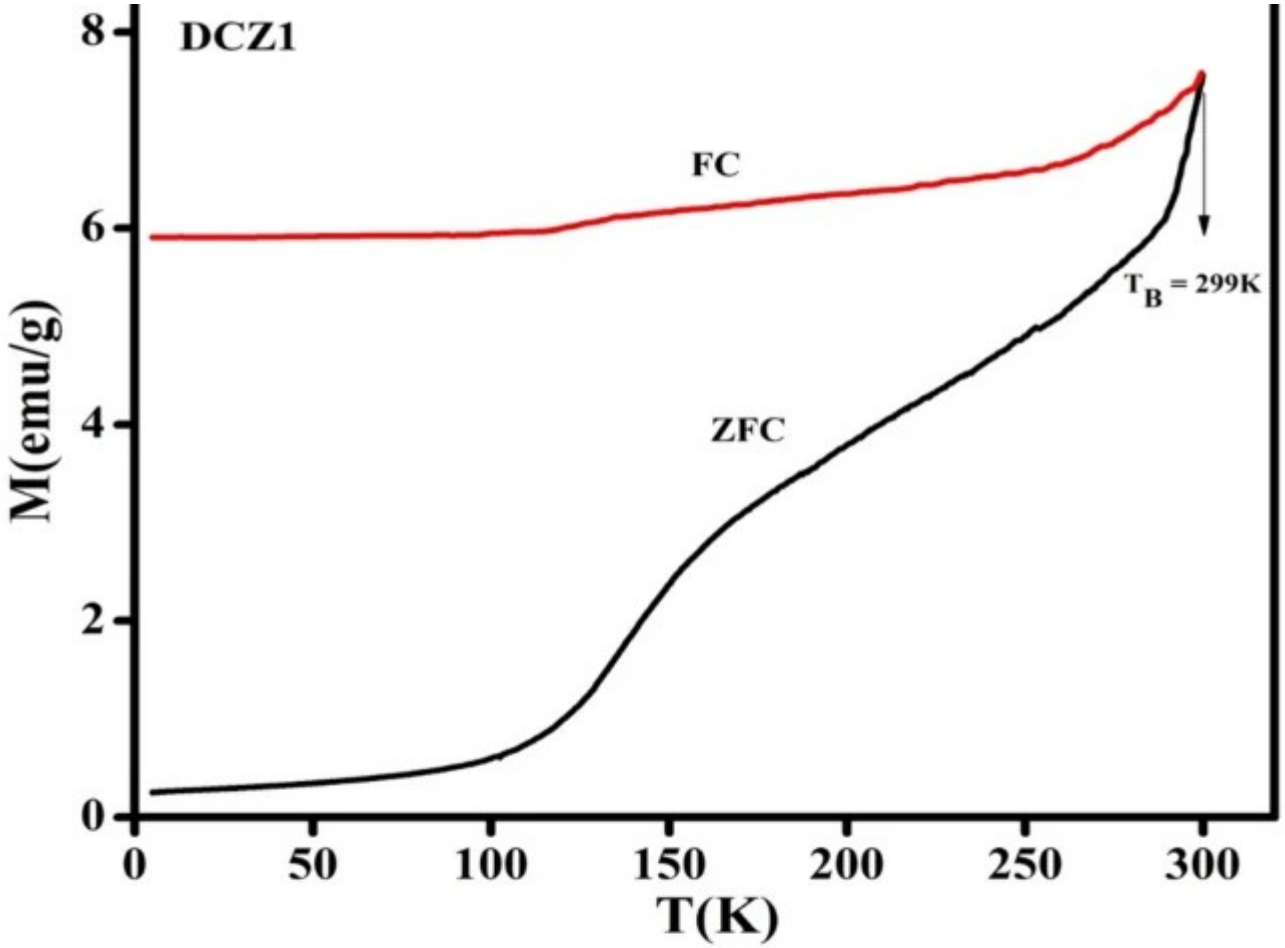
DCZ1
FC
ZFC
T_B = 299K
M(emu/g)
T(K)
0
2
4
6
8
0
50
100
150
200
250
300

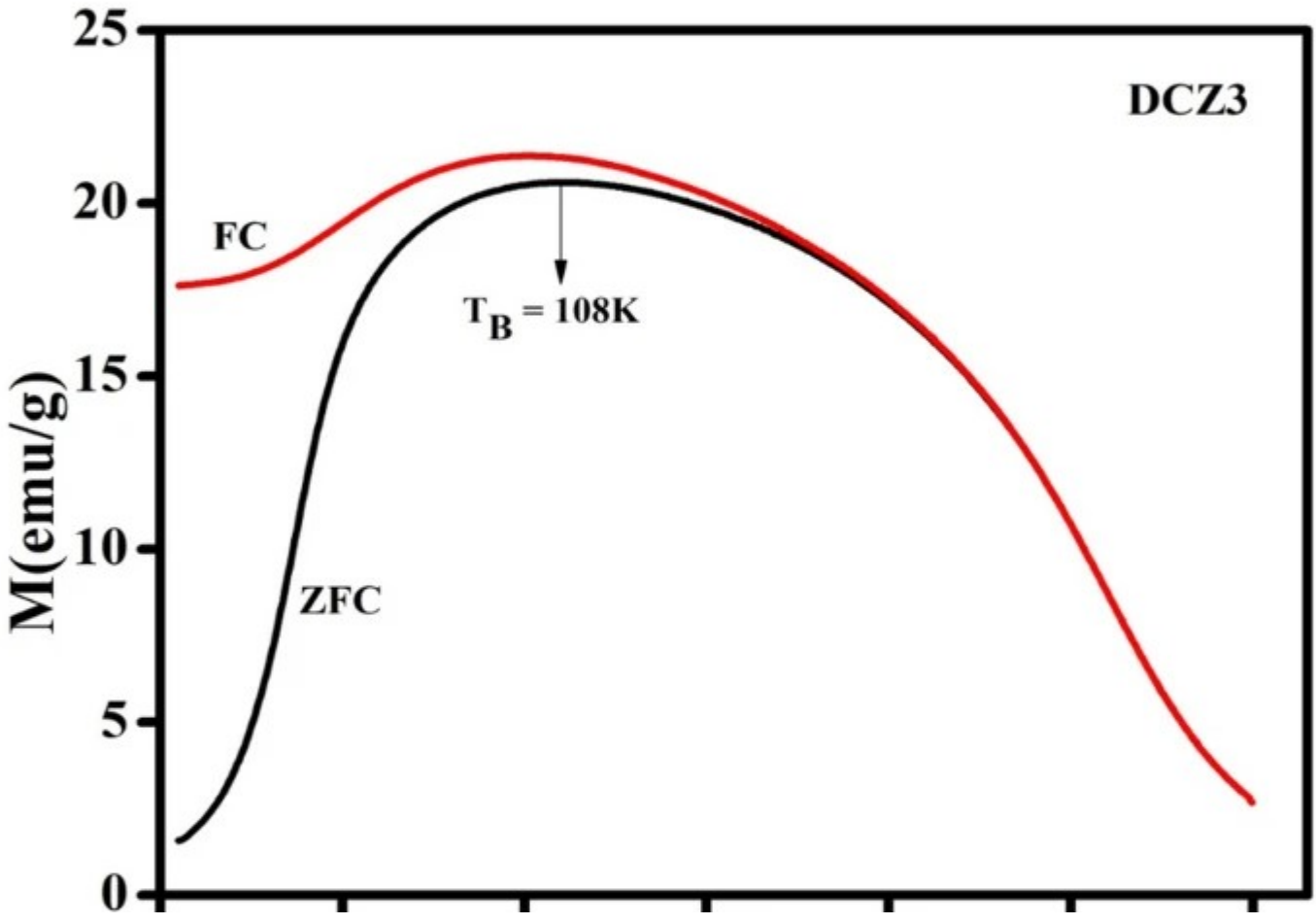
DCZ3
FC
ZFC
T_B = 108K
M(emu/g)
0
5
10
15
20
25

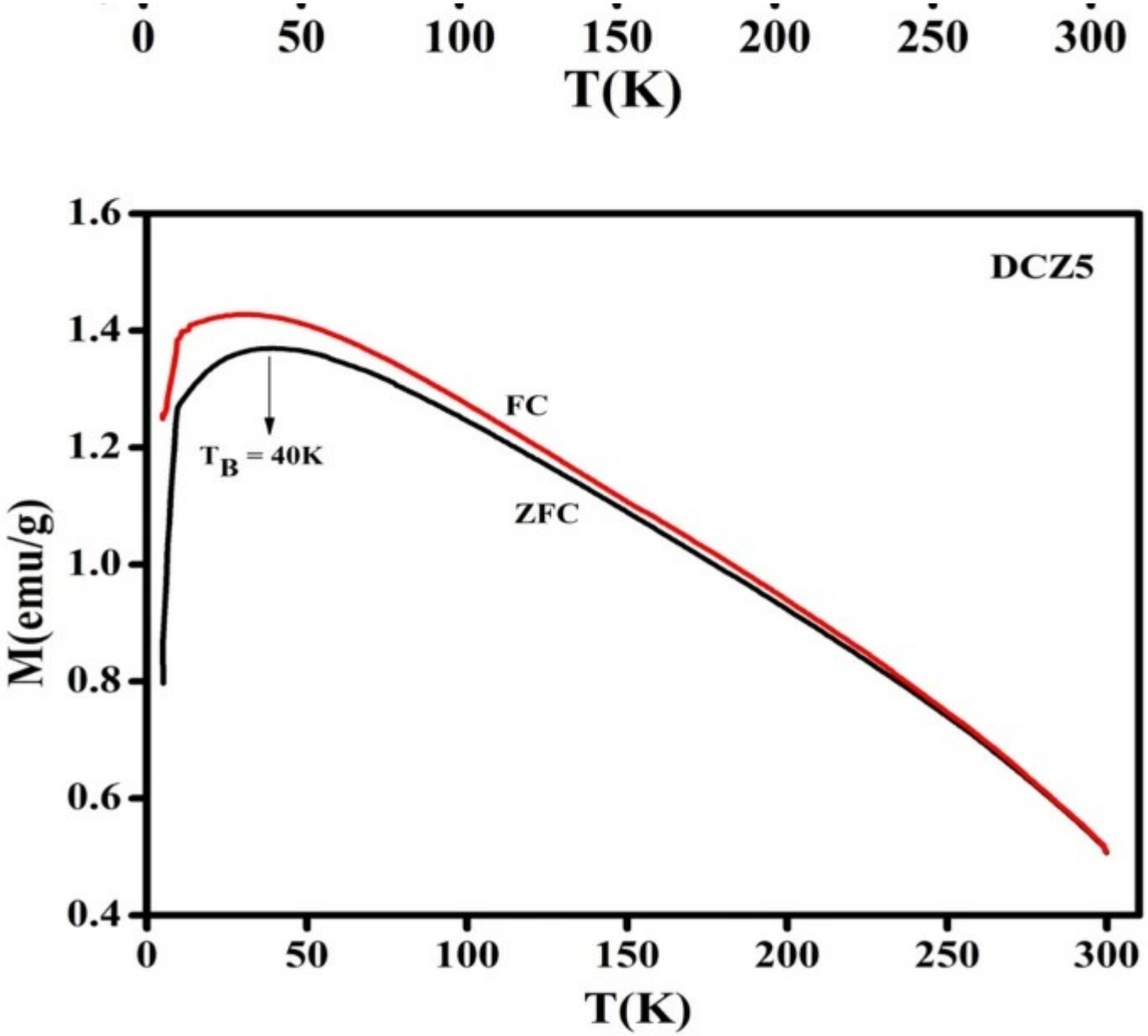

ZFC–FC curves of DCZ1, DCZ3 and DCZ5 samples under applied magnetic field 500 Oe

The calculated blocking temperature of DCZ1, DCZ3 and DCZ5 nanoparticles from the FC–ZFC curve is 299 K, 108 K and 40 K, respectively, as shown in Table 6. The blocking temperature of samples shifted toward a lower temperature with incrementing Zn content in cobalt ferrite because of the effect of the particle size on the temperature. DCZ1 curve indicates that cobalt ferrite NPs show ferromagnetic at lower temperature and superparamagnetic behavior above 300 K. Ahmad et al. have reported that the ferromagnetism and superparamagnetism of the NPs are the characteristic property of T_B, which depends on the applied magnetic field at which measurement is carried out and also on the particle size [54]. An FC–ZFC measurement

of DCZ3 and DCZ5 samples indicates irretrievable magnetic nature underneath the temperature, which is known as irreversibility (T_{irr}) temperature. DCZ3 and DCZ5 samples show superparamagnetic behavior because it is the characteristic of superparamagnetic material; the magnetization monotonically decreases with increasing temperature above the T_B in the unblocked region. The comparative study of results obtained from M–H and M–T analysis indicates that DCZ3 sample shows some excellent properties of magnetism as compared to the remaining two samples, which are necessary in the case of biomedical application.

4 Conclusion

DCZ1, DCZ3 and DCZ5 NPs with phase pure cubic spinel structure were prepared by a cost-effective co-precipitation route. Thermal studies revealed the minimum total weight loss observed during the formation of the spinel phase and also superior stability of the prepared sample at a higher temperature range. Apart from Rietveld refinement of NPs that verified the monophasic cubic structure, there are also no other new phases observed. The χ^2 value for all analyzed samples is found to be closer to 1, suggesting the goodness of fit. The crystallite size of samples calculated by both Scherrer's formula and W–H methods was found to be in good agreement with each other. The crystallite size of samples has been observed to be increased from 22 to 29 nm with Zn doping perhaps because Zn^{2+} has larger ionic radii as compared to Co^{2+}. The FE-SEM analysis reveals agglomeration between the particles, which decreases after zinc incorporation. Best-fitted Raman spectra verified the spinel structure of prepared NPs. The values of Raman modes were observed to be increased after the incorporation of zinc, which revealed that the particle size and the values of Raman mode show direct proportionality. The magnetic parameters such as M_s, H_c, M_r, M_r/M_s and n_B decreased with increasing Zn doping. The FC and ZFC curve of samples reveals that the blocking temperature of samples decreases with increasing zinc concentration in Co-ferrite NPs. The study of both FC-ZFC and M-H loop indicates the samples $0.5 \leq x \leq 1$ show superparamagnetic behavior at room temperature. The result of all characterization techniques in this paper concluded that the structural, morphological and magnetic properties of cobalt ferrite nanomaterials can be suitably modified by doping with Zn^{2+}. Hence, these materials are promising and also good candidates in the case of biomedical application; particularly, these ferrites are desirable

material for magnetic hyperthermia applications.

References

1. J.K. Patra et al., Nano based drug delivery systems: recent developments and future prospects. J. Nanobiotechnol. 16(1), 71 (2018)

Article Google Scholar

2. A. Minnich et al., Bulk nanostructured thermoelectric materials: current research and future prospects. Energy Environ. Sci. 2(5), 466–479 (2009)

Article Google Scholar

3. J.H. Belo et al., Magnetocaloric materials: from micro-to nanoscale. J. Mater. Res. 34(1), 134–157 (2019)

Article ADS Google Scholar

4. H. Heinz et al., Nanoparticle decoration with surfactants: molecular interactions, assembly, and applications. Surf. Sci. Rep. 72(1), 1–58 (2017)

Article ADS Google Scholar

5. S.R. Patade et al., Self-heating evaluation of superparamagnetic MnFe2O4 nanoparticles for magnetic fluid hyperthermia application towards cancer treatment. Ceram. Int. 46(16), 25576–25583 (2020)

Article Google Scholar

6. S.A. Jadhav, S.B. Somvanshi, M.V. Khedkar, S.R. Patade, K.M. Jadhav, Magneto-structural and photocatalytic behavior of mixed Ni–Zn nano-spinel ferrites: visible light-enabled

active photodegradation of rhodamine B. J. Mater. Sci.: Mater. Electron. 31, 11352–11365 (2020)

Google Scholar

7. Sun, J. Z., *Current-induced magnetic switching device and memory including the same*. 2001, Google Patents

8. E.R. Kumar et al., Synthesis of Mn substituted CuFe2O4 nanoparticles for liquefied petroleum gas sensor applications. Sens. Actuators B Chem. 191, 186–191 (2014)

Article Google Scholar

9. H. Shao et al., Magnetic nanoparticles and microNMR for diagnostic applications. Theranostics 2(1), 55 (2012)

Article Google Scholar

10. S.B. Somvanshi et al., Influential diamagnetic magnesium (Mg2+) ion substitution in nano-spinel zinc ferrite (ZnFe2O4): thermal, structural, spectral, optical and physisorption analysis. Ceram. Int. 46(7), 8640–8650 (2020)

Article Google Scholar

11. A.N. Birgani, M. Niyaifar, A. Hasanpour, Study of cation distribution of spinel zinc nano-ferrite by X-ray. J. Magn. Magn. Mater. 374, 179–181 (2015)

Article ADS Google Scholar

12. M. Srivastava et al., Influence of pH on structural morphology and magnetic properties of ordered phase cobalt doped lithium ferrites nanoparticles synthesized by sol–gel method. Mater. Sci. Eng. B 175(1), 14–21 (2010)

Article Google Scholar

13. M. Houshiar et al., Synthesis of cobalt ferrite (CoFe2O4) nanoparticles using combustion, coprecipitation, and precipitation methods: a comparison study of size, structural, and magnetic properties. J. Magn. Magn. Mater. 371, 43–48 (2014)

Article ADS Google Scholar

14. K. Sinkó et al., Liquid-phase syntheses of cobalt ferrite nanoparticles. J. Nanopart. Res. 14(6), 894 (2012)

Article ADS Google Scholar

15. L.C. Sonia, M. Victory, S. Phanjoubam, Effect of synthesis technique on thestructural, electrical and magnetic properties ofzinc nanoferrite. Int. J. Sci. Eng. Res. 8(5), 5–10 (2017)

Google Scholar

16. Z. Wang et al., A facile co-precipitation synthesis of robust FeCo phosphate electrocatalysts for efficient oxygen evolution. Electrochim. Acta 264, 244–250 (2018)

Article ADS Google Scholar

17. K. Maaz et al., Synthesis and magnetic characterization of nickel ferrite nanoparticles prepared by co-precipitation route. J. Magn. Magn. Mater. 321(12), 1838–1842 (2009)

Article ADS Google Scholar

18. V.S. Kiran, S. Sumathi, Comparison of catalytic activity of bismuth substituted cobalt ferrite nanoparticles synthesized by combustion and co-precipitation method. J. Magn.

Magn. Mater. 421, 113–119 (2017)

Article ADS Google Scholar

19. B. Toksha et al., Structural investigations and magnetic properties of cobalt ferrite nanoparticles prepared by sol–gel auto combustion method. Solid State Commun. 147(11–12), 479–483 (2008)

Article ADS Google Scholar

20. S. Jauhar et al., Tuning the properties of cobalt ferrite: a road towards diverse applications. RSC Adv. 6(100), 97694–97719 (2016)

Article ADS Google Scholar

21. M.M. Naik et al., Effect of aluminium doping on structural, optical, photocatalytic and antibacterial activity on nickel ferrite nanoparticles by sol–gel auto-combustion method. J. Mater. Sci. Mater. Electron. 29(23), 20395–20414 (2018)

Article Google Scholar

22. M. Namdeo et al., Magnetic nanoparticles for drug delivery applications. J. Nanosci. Nanotechnol. 8(7), 3247–3271 (2008)

Article Google Scholar

23. H. Yun, Synthesis and characterization of transition metal based metal oxide and metallic nanocrystals for AC magnetic devices and catalysis. Synthesis 1, 1–2015 (2015)

Google Scholar

24. P. Coppola et al., Hydrothermal synthesis of mixed zinc–cobalt ferrite nanoparticles:

structural and magnetic properties. J. Nanopart. Res. 18(5), 138 (2016)

Article ADS Google Scholar

25. H. Shokrollahi, Structure, synthetic methods, magnetic properties and biomedical applications of ferrofluids. Mater. Sci. Eng., C 33(5), 2476–2487 (2013)

Article Google Scholar

26. M.B. Ali et al., Effect of zinc concentration on the structural and magnetic properties of mixed Co–Zn ferrites nanoparticles synthesized by sol/gel method. J. Magn. Magn. Mater. 398, 20–25 (2016)

Article ADS Google Scholar

27. H. Kaur et al., Structural, thermal and magnetic investigations of cobalt ferrite doped with Zn2+ and Cd2+ synthesized by auto combustion method. J. Magn. Magn. Mater. 474, 505–511 (2019)

Article ADS Google Scholar

28. B.J. Rani et al., Pure and cobalt-substituted zinc-ferrite magnetic ceramics for supercapacitor applications. Appl. Phys. A 124(7), 1–12 (2018)

Article ADS Google Scholar

29. K. Anu, J. Hemalatha, Magnetic and electrical conductivity studies of zinc doped cobalt ferrite nanofluids. J. Mol. Liq. 284, 445–453 (2019)

Article Google Scholar

30. R.S. Yadav et al., Structural, magnetic, elastic, dielectric and electrical properties of hot-

press sintered Co1-xZnxFe2O4 (x= 0.0, 0.5) spinel ferrite nanoparticles. J. Magn. Magn. Mater. 447, 48–57 (2018)

Article ADS Google Scholar

31. S. Ansari et al., Cobalt nanoparticles for biomedical applications: facile synthesis, physiochemical characterization, cytotoxicity behavior and biocompatibility. Appl. Surf. Sci. 414, 171–187 (2017)

Article ADS Google Scholar

32. A. Hadela et al., Novel reusable functionalized magnetic cobalt ferrite nanoparticles as oil adsorbents. Adsorpt. Sci. Technol. 38(5–6), 168–190 (2020)

Article Google Scholar

33. M.M. Naik et al., Green synthesis of zinc doped cobalt ferrite nanoparticles: structural, optical, photocatalytic and antibacterial studies. Nano-Struct. Nano-Objects 19, 100322 (2019)

Article Google Scholar

34. B. Peeples et al., Structural, stability, magnetic, and toxicity studies of nanocrystalline iron oxide and cobalt ferrites for biomedical applications. J. Nanopart. Res. 16(2), 2290 (2014)

Article ADS Google Scholar

35. E. Bagherzadeh, H.R.M. Hosseini, J. Khakzadian, Synthesis of magnetic mesoporous nanocomposites: a promising candidate for diagnostic and therapeutic biomedical applications. Mater. Chem. Phys. 167, 201–208 (2015)

Article Google Scholar

36. J.S. Kounsalye et al., Rietveld, cation distribution and elastic investigations of nanocrystalline Li0. 5+ 0.5 xZrxFe2. 5-1.5 xO4 synthesized via sol–gel route. Phys. B Condens. Matter 547, 64–71 (2018)

Article ADS Google Scholar

37. D. Jnaneshwara et al., Effect of zinc substitution on the nanocobalt ferrite powders for nanoelectronic devices. J. Alloy. Compd. 587, 50–58 (2014)

Article Google Scholar

38. M. Irfan et al., Structural and magnetic properties of Fe3Ga alloy nanowires: effect of post annealing treatment. J. Alloy. Compd. 691, 1–7 (2017)

Article Google Scholar

39. J.S. Kounsalye et al., Influence of Ti 4+ ion substitution on structural, electrical and dielectric properties of Li 0.5 Fe 2.5 O 4 nanoparticles. J. Mater. Sci. Mater. Electron. 28(22), 17254–17261 (2017)

Article Google Scholar

40. V. Vinayak et al., Structural, microstructural, and magnetic studies on magnesium (Mg 2+)-substituted CoFe 2 O 4 nanoparticles. J. Supercond. Novel Magn. 29(4), 1025–1032 (2016)

Article Google Scholar

41. D. Nath, F. Singh, R. Das, X-ray diffraction analysis by Williamson-Hall, Halder-Wagner and size-strain plot methods of CdSe nanoparticles-a comparative study. Mater. Chem. Phys. 239, 122021 (2020)

Article Google Scholar

42. S. Gul et al., Al-substituted zinc spinel ferrite nanoparticles: preparation and evaluation of structural, electrical, magnetic and photocatalytic properties. Ceram. Int. 46(9), 14195–14205 (2020)

Article Google Scholar

43. W.L. de Almeida et al., Study of structural and optical properties of ZnO nanoparticles synthesized by an eco-friendly tapioca-assisted route. Mater. Chem. Phys. 258, 123926 (2021)

Article Google Scholar

44. L. Kumar, P. Kumar, M. Kar, Cation distribution by Rietveld technique and magnetocrystalline anisotropy of Zn substituted nanocrystalline cobalt ferrite. J. Alloy. Compd. 551, 72–81 (2013)

Article Google Scholar

45. M. Beyranvand, A. Gholizadeh, Structural, magnetic, elastic, and dielectric properties of Mn 0.3−x Cd x Cu 0.2 Zn 0.5 Fe 2 O 4 nanoparticles. J. Mater. Sci. Mater. Electron. 31(7),

5124–5140 (2020)

Article Google Scholar

46. R.S. Yadav et al., Magnetic properties of Co1-xZnxFe2O4 spinel ferrite nanoparticles synthesized by starch-assisted sol–gel autocombustion method and its ball milling. J. Magn. Magn. Mater. 378, 190–199 (2015)

Article ADS Google Scholar

47. A.V. Humbe et al., Impact of Jahn Teller ion on magnetic and semiconducting behaviour of Ni-Zn spinel ferrite synthesized by nitrate-citrate route. J. Alloy. Compd. 691, 343–354 (2017)

Article Google Scholar

48. N. Sanpo, C.C. Berndt, J. Wang, Microstructural and antibacterial properties of zinc-substituted cobalt ferrite nanopowders synthesized by sol–gel methods. J. Appl. Phys. 112(8), 084333 (2012)

Article ADS Google Scholar

49. N. Somaiah et al., Magnetic and magnetoelastic properties of Zn-doped cobalt-ferrites—CoFe2-xZnxO4 (x= 0, 0.1, 0.2, and 0.3). J. Magn Magn Mater 324(14), 2286–2291 (2012)

Article ADS Google Scholar

50. D.D. Andhare et al., Effect of Zn doping on structural, magnetic and optical properties of cobalt ferrite nanoparticles synthesized via Co-precipitation method. Phys. B Conden. Matter 583, 412051 (2020)

Article Google Scholar

51. G. Aravind, M. Raghasudha, D. Ravinder, Synthesis, characterization and FC–ZFC magnetization studies of cobalt substituted lithium nano ferrites. J. Magn. Magn. Mater. 378, 278–284 (2015)

Article ADS Google Scholar

52. K. Praveena, K. Sadhana, Ferromagnetic properties of Zn substituted spinel ferrites for high frequency applications. Int. J. Sci. Res. Publ. 5(4), 1–21 (2015)

Google Scholar

53. W. Mohamed et al., Impact of Co2+ substitution on microstructure and magnetic properties of coxzn1-xfe2o4 nanoparticles. Nanomaterials 9(11), 1602 (2019)

Article Google Scholar

54. S.I. Ahmad et al., Dielectric, impedance, AC conductivity and low-temperature magnetic studies of Ce and Sm co-substituted nanocrystalline cobalt ferrite. J. Magn. Magn. Mater. 492, 165666 (2019)

Article Google Scholar

Acknowledgements

The author Deepali D. Andhare acknowledges Chhatrapati Shahu Maharaj Research, Training and Human Development Institute (SARTHI) Pune, Government of Maharashtra, for the financial support under CMSRF-2019. The author is thankful to Dr. Alok Banerjee and Dr. Vasant Sathe Scientists UGC-DAE Consortium for Scientific Research, Indore, India, for providing VSM measurement and Raman facilities, respectively.

Author information

Authors and Affiliations

Department of Physics, Dr. Babasaheb Ambedkar Marathwada University, Aurangabad, Maharashtra, 431004, India
Deepali D. Andhare, Supriya R. Patade, Swapnil A. Jadhav, Sandeep B. Somvanshi & K. M. Jadhav

Corresponding author

Correspondence to K. M. Jadhav.

Ethics declarations

Conflict of interest

There are no conflicts of interest connected to the present work.

Additional information

Publisher's Note

Rights and permissions

About this article

Cite this article

Andhare, D.D., Patade, S.R., Jadhav, S.A. *et al.* Rietveld refined structural, morphological, Raman and magnetic investigations of superparamagnetic Zn–Co nanospinel ferrites prepared by cost-effective co-precipitation route. *Appl. Phys. A* 127, 480 (2021). https://doi.org/10.1007/s00339-021-04603-9

Received	Accepted	Published
28 February 2021	15 May 2021	01 June 2021

DOI
https://doi.org/10.1007/s00339-021-04603-9

Share this article

Anyone you share the following link with will be able to read this content:

Get shareable link

Keywords

Co-precipitation Rietveld refinement Raman peak fitting

Cobalt–zinc ferrite Magnetic properties